Naval Research Laboratory

Washington, DC 20375-5320

NRL/FR/7420--97-9848

Fundamentals of Acoustic Backscatter Imagery

CLYDE E. NISHIMURA

Marine Physics Branch
Marine Geosciences Division

October 20, 1997

REPORT DOCUMENTATION PAGE

Form Approved
OMB No. 0704-0188

1. AGENCY USE ONLY *(Leave Blank)*	2. REPORT DATE	3. REPORT TYPE AND DATES COVERED
	October 20, 1997	Final Report, October 1995-September 1996

4. TITLE AND SUBTITLE

Fundamentals of Acoustic Backscatter Imagery

5. FUNDING NUMBERS

PE - 0305139B

6. AUTHOR(S)

Clyde E. Nishimura

7. PERFORMING ORGANIZATION NAME(S) AND ADDRESS(ES)

Naval Research Laboratory
Washington, DC 20375-5320

8. PERFORMING ORGANIZATION REPORT NUMBER

NRL/FR/7420--97-9848

9. SPONSORING/MONITORING AGENCY NAME(S) AND ADDRESS(ES)

National Imagery and Mapping Agency
4600 Sangamore Road
Bethesda, MD 20816

10.SPONSORING/MONITORING AGENCY REPORT NUMBER

11. SUPPLEMENTARY NOTES

12a. DISTRIBUTION/AVAILABILITY STATEMENT

Approved for public release; distribution is unlimited.

12b. DISTRIBUTION CODE

13. ABSTRACT *(Maximum 200 words)*

This report summarizes various multidisplinary subjects that play an important role in the operation, processing, and interpretation of acoustic backscattering systems and their data. The subject matter covered includes the physics of wave propagation and scattering, basic imaging system engineering, mode of standard survey operations, processing methodology, and marine geology and geophysics.

14. SUBJECT TERMS

Acoustic backscatter
Sidescan
Multibeam
Acoustic imagery

15. NUMBER OF PAGES

71

16. PRICE CODE

17. SECURITY CLASSIFICATION OF REPORT	18. SECURITY CLASSIFICATION OF THIS PAGE	19. SECURITY CLASSIFICATION OF ABSTRACT	20. LIMITATION OF ABSTRACT
UNCLASSIFIED	UNCLASSIFIED	UNCLASSIFIED	UL

NSN 7540-01-280-5500

Standard Form 298 (Rev. 2-89)
Prescribed by ANSI Std 239-18
298-102

CONTENTS

FUNDAMENTALS OF ACOUSTIC BACKSCATTER IMAGERY

1. INTRODUCTION

Acoustic imagery of the seafloor, generated from either multibeam or towed sidescan sonar systems, represent the received acoustic backscattered intensity. These acoustic intensities depend on the scattering strength of the seafloor, distribution of scatterers, degree of bottom penetration and sub-bottom volume scattering, and ensonification angle. When properly interpreted, acoustic imagery can provide details about the seafloor that cannot be easily extrapolated from knowledge of the seafloor bathymetry.

Acoustic backscatter imagery is used in a diverse set of applications and disciplines ranging from geological mapping to the detection of manmade objects on the seafloor. As such, acoustic backscatter imagery has many naval applications that include obstacle avoidance, characterization of the type of seafloor for engineering purposes, mine detection, and parameterization of the seafloor for acoustic propagation modeling.

The proper interpretation of acoustic backscatter imagery data requires that the analyst understand a wide range of topics: the physics of wave propagation and scattering, basic imaging system engineering, mode of standard survey operations, processing methodology, and marine geology and geophysics. The diversity of these subjects is certainly non-trivial. It is therefore understandable that many first-time end-users of imagery data lack a fundamental understanding of all of these topics.

This report summarizes various aspects of backscatter acoustic imagery. While most of the emphasis and examples used in this review focus on low frequency (< 20 kHz) systems, the salient principles presented apply to the whole range of instrumentation. While this treatise is not all inclusive, it attempts to touch upon the various aspects that play an important role in the operation of acoustic backscatter imaging systems and in the interpretation of the imagery data. This report augments the outstanding review article of Somers and Stubbs [1], which is the best comprehensive source of information on the design aspects of sidescan systems. Additional information about seafloor mapping can also be found in several other review articles [2-8].

This report was written in support of the Hydrographic Source Assessment System (HYSAS) program managed by the Joint Program Office (JPO). The JPO is an intergovernment agency group consisting of members from the Defense Mapping Agency (now NIMA, National Imagery and Mapping Agency), Naval Oceanographic Office (NAVOCEANO), and National Oceanographic and Atmospheric Administration (NOAA). The Marine Physics Branch of the Naval Research Laboratory was tasked at providing technical advice as to the implementation in HYSAS of the acoustic imagery layer of the Master Seafloor Digital Database (MSDDB).

Manuscript approved December 19, 1996

1.1 Historical Background

The use of sidescan sonar for search and geological mapping dates back to the late 1950s with the realization that acoustic backscatter reverberation could be used for mapping the seafloor [9-13]. This led to the initial development and use of sidescan sonar systems, primarily by the British [14-16]. Subsequent U.S. development of these capabilities followed shortly in the early 1960s [1], and somewhat accelerated after the loss of the USS *Thresher* in 1963. It is interesting to note that the first scientific paper published in the U.S. that used sidescan data was an interpretation of the geology in the *Thresher* search area [17].

All these early systems operated at frequencies above 30 kHz and were therefore limited in their range capabilities. In many cases, these systems were also constrained to a shallow depth deployment, thereby limiting their use to offshore continental shelf waters. It was not until the development of GLORIA by the Institute of Oceanographic Sciences that a low-frequency (~6 kHz) system was available that was capable of wide swath, full ocean depth surveying [18-21]. To date, the most impressive surveying task performed by a sidescan system was the mapping of the entire U.S. 200 mile Exclusive Economic Zone by GLORIA (e.g., Refs. 22 and 23). Over 7 million square kilometers of the seafloor were imaged successfully.

The development of sidescan systems capable of also collecting bathymetric data followed on a serendipitous discovery. Early users of sidescan systems noticed that interference patterns were sometimes observed while surveying in calm sea-state conditions. These interference fringes were correctly ascribed to be a Lloyd mirror effect created by the reception of the coherent reflection of the return signal from the sea surface [24, 25]. Subsequent attempts were made to replicate this effect by using reflecting plates mounted to the towfish [26]. In time, it was realized that a second or third parallel array could be used instead to produce an interferometric system [27, 28]. This latter development was incorporated into the low-frequency SeaMARC II sidescan system in the early

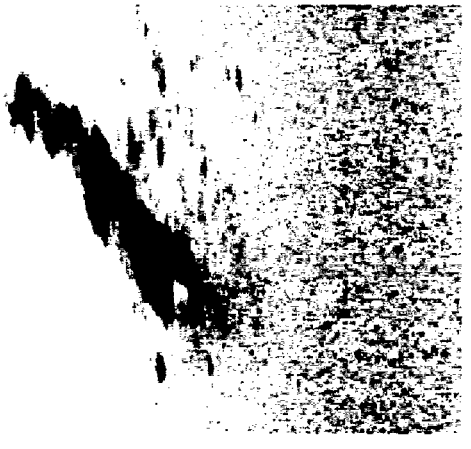

Fig. 1 — Target identification example. This 70 kHz TAMU[2] sidescan image of the wreck of a cargo ship located in the Straits of Juan de Fuca indicates stronger backscattered signals via darker gray levels. Ensonification direction is from right to left, and width of the area imaged is approximately 180 m. Note the presence of debris around the wreck.

1980s [29-31], and recently into the GLORI-B system [32, 33]. This capability is referred to in the literature as either swath bathymetry or bathymetric sidescan.

The first effective multibeam systems were deployed starting with the initial SASS [34], which was implemented in 1965 by the Harris ASW Division of General Instruments. Since they were first sold to the commercial and academic communities in the 1970s, multibeam systems have been the key component to mapping the bathymetric relief of the seafloor. This past decade has witnessed the practical implementation of collecting acoustic backscatter imagery data using multibeam bathymetric systems. Starting with the work of deMoustier using SeaBeam data [35-38], this capability now exists for nearly all low-frequency multibeams including SeaBeam2100 [39], HYDROSWEEP, Simrad12A and EM12 [40, 41], and SASS Phase IV [42, 43]. This recent development will continue to improve in the next decade.

Since their inception, sidescan sonars have been the mainstay of wide-area search missions for manmade objects on the seafloor. The list of notable achievements is long and distinguished, and include the location of the submersible *ALVIN* in 1968, the *Titanic*, and the debris from the Space Shuttle *Challenger* explosion. Sidescan systems are also a stalwart component of mine hunting equipment including the U.S. Navy's MK24 Mod 0 underwater ordnance locator, AN/AQS-14, and AN/SQQ-14. The niche that high-frequency sidescan occupies in its ability to survey an area wider than that viewable by optical imaging, while maintaining a spatial resolution better than that of multibeam systems, ensures the continual use of sidescan instruments well into the 21st century.

2. ACOUSTIC PROPAGATION

Several aspects of acoustic propagation influence the design of acoustic instrumentation, survey operations, and acoustic imagery data. This section briefly reviews some these topics. The interested reader can find a more comprehensive review of ocean acoustics in several useful books [44-46].

2.1 Source Pressure Level

The standard unit of measure for the sound intensity or pressure level in the oceans is the decibel. Unfortunately, there is much confusion in the scientific and technical literature concerning the usage of this term [47]. Historically, the decibel (dB) was initially used to indicate power levels during electrical transmissions and was defined as

$$\text{power transmission ratio (dB)} = 10 \log_{10} (W_2 / W_1) ,$$

where W_1 and W_2 are the input and transmitted power, respectively. In this case, power was a directly measurable quantity.

The acoustic community eventually adopted the use of the decibel as a means of describing sound pressure levels. However, the use of a power reference value in the definition of a decibel necessitates converting pressure, which is measurable, to power, which is estimated based on an assumed mode of propagation. Furthermore, it is common in acoustics to use intensity, which is the power per unit area of an acoustic wave. For the case of a spherical wave from a continuous sinusoidal point source, the intensity I is given by

$$I = P^2 / (2 \rho c r^2) , \qquad (1)$$

where P is the average pressure, ρ is the density, r is the distance radius, and c the sound speed of the media. For a propagating plane wave, the intensity is

$$I = P^2 / (2 \rho c),$$

with the difference between the absence of the geometrical spreading $1/r^2$ factor for the spherical wave.

It is common practice to characterize acoustic imaging systems by their source levels in units of dBs; this then requires the selection of a reference power value. However, intensity can be used instead of power by specifying both a reference distance and a propagation model; the current standard distance is one meter. Assuming some reference intensity level at one meter range and spherical propagation from a point source, Eq. (1) reduces to

$$I_{ref} = P_{ref}^2 / (2 \rho c),$$

where the subscript *ref* denotes reference values. The source level ratio is simply given by

$$\text{Source Level Ratio} = I / I_{ref} = (P / P_{ref})^2.$$

Since acoustic pressure is usually the measured quantity, it is therefore convenient to specify a reference pressure value rather than a reference intensity value. In the early 1970s, the U.S. Navy selected one micropascal (μPa) to be the reference pressure. The definition of a source level in decibels is therefore

$$\text{Source Level} = 20 \log_{10}(P / P_{ref}) \quad \text{dB re [} (\mu\text{Pa}) \text{ @ 1 m]} \tag{2}$$

$$\text{Source Level} = 10 \log_{10}(I / I_{ref}) \quad \text{dB re [} (\mu\text{Pa}) \text{ @ 1 m]}, \tag{3}$$

where re [(μPa) @ 1 m] means with respect to one μPa at 1 m distance.

It is important to remember the assumptions inherent in this derivation. Pressure is defined as the average pressure from a time continuous, point source. The use of a reference distance in conjunction with the mode of propagation is also critical. The source level should be the pressure that would be measured at one meter distance from an ideal point source in any direction (spherical propagation).

It is sometimes more informative to write the definition of dB with respect to some reference power; the standard unit for power is one Watt (W). Using a water density of 1.5 gm/cm^3, and a sound speed of 1.5 km/s, we can derive from Eq. (1) that a reference pressure, I_{ref} of 1 μPa, corresponds to 0.67×10^{-18} W/m^2. Assuming spherical spreading, the one meter distance reference frame, and the definition of dB (Eq. (3)), one can derive that

$$\text{Source Level re [} (\mu\text{Pa}) \text{ @ 1 m]} = 171 \text{ dB} + 10 \log_{10}(E_w), \tag{4}$$

where E_w is the power in units of watts.

2.2 Sonar Equation

Backscatter acoustic imagery data represents the return signal from the seafloor that was ensonified by an acoustic source. The strength of this received signal can be represented by the sonar equation

$$RS = SL + DI - 2\,TL - NL + TS\,, \tag{5}$$

where *RS* is the received signal level, *DI* is the receiver directivity index (deviation from spherical spreading), *SL* is the source level, *TL* is the transmission loss, *NL* is noise, and *TS* is the target strength. All the variables in this sonar equation are given in dBs. For the case of seafloor mapping, the *TL* component is multiplied by 2 to indicate the two-way (receiver/target) travel path. *TL* is composed of two separate terms

$$TL = GS + AT\,,$$

where *GS* is geometric spreading and *AT* is attenuation (absorption). The components of *TL* are further explored in Sections 2.2.1 and 2.2.2.

2.2.1 Attenuation

The propagation of acoustic energy is characterized by frequency dependent attenuation. In an absorptive medium such as seawater, this results in a reduction of a fraction of energy per distance traveled. For the case of simple plane wave propagation

$$\frac{dI(r)}{I(r)} = -\beta\, dr\,, \tag{6}$$

where r is the distance traveled, $I(r)$ is the intensity, and β is some attenuation factor that is frequency dependent. The solution to Eq. (6) is simply

$$I(r) = I_o \exp(-\beta r)\,.$$

Taking the ratio of $I(r) / I_o$ and then converting to decibels units yields an expression in terms of the attenuation coefficient α

$$TL_{absorption} = 10 \log [\exp(\beta r)] = \alpha r\,,$$

where α is equal to [β 10 $\log_{10}(\varepsilon)$], and ε is the base of natural logarithms.

It is well known that three frequency-dependent processes control attenuation in the oceans (Fig. 2). For frequencies above 1000 kHz, viscous shear is the dominant process. Its absorption coefficient α is given by [48]

$$\alpha = \frac{16\pi^2 \mu_s}{3\rho c^3} f^2,$$

where μ_s is the shear viscosity (poise), ρ is the density (g/cm^3), c is the sound speed (cm/s), and f is the frequency (Hz).

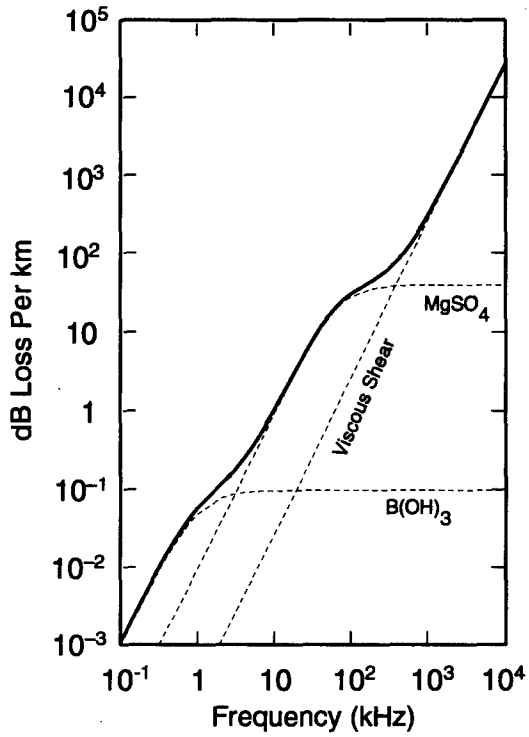

Fig. 2 — Absorption coefficient as a function of frequency. The dashed lines represent the three different processes that control absorption.

In the frequency range 1 to 100 kHz ionic relaxation, the result of the dissociation of magnesium sulfate ($MgSO_4$) is the dominant process [49]. In this case, the propagation of acoustic waves results in the breakdown of $MgSO_4$ followed by quick reassociation. At frequencies below 1 kHz, boric acid, $B(OH)_3$, ionization processes are the main contributing factor; this latter process is dependent on the pH and thus varies between oceans. Finally, one should note that acoustic attenuation in fresh water is only affected by the viscous shear component.

2.2.2 Geometric Spreading

The propagation of acoustic energy results in the systematic decrease in intensity due to the spreading of this energy over a greater area. This loss is termed geometric spreading and is deterministic for the acoustic imaging systems described in this report. For the case of short range imaging, acoustic energy spreads out in all directions. Therefore, this loss is spherical and is described by the inverse square law (surface area of a sphere)

$$I(r) = I_o\, r^2,$$

or in terms of dB loss by

$$TL_{spreading} = 20 \log(r)\ ,$$

where r is in units of meters. Because the speed of sound in water is nearly a constant, this loss is equivalent to an inverse squared time relationship.

2.3 Sound Speed

The speed of sound in the oceans depends on temperature, salinity, and depth-dependent hydrostatic pressure. One empirical formula that describes this relationship is

$$c = 1449 + 4.64\,T - 0.055\,T^2 + 0.0003\,T^3 + (1.39 - 0.012\,T)\,(S - 35) + 0.017\,Z,$$

where c is the sound speed (m/s), T is the temperature (°C), S is the salinity (parts per thousand), and Z is the depth (m).

At shallow depths ($Z \approx 0$), temperature is obviously the most important parameter in determining the sound speed. In much of the world's oceans, there exist large seasonal temperature changes in the uppermost depths, an area called the surface thermocline region. During the summer months, the thermocline is characterized by a large vertical temperature gradient, which then produces a relatively large change in the sound speed.

On the other hand, temperature is essentially a constant at depths greater than 1400 m. At these greater depths, hydrostatic pressure becomes the dominant factor. This results in an increase in speed of 17 m/s for every 1 km increase in depth. Finally, except in exceptional areas such as the western approaches to the Straits of Gibraltar or in shallow water estuaries, salinity is essentially a constant and does not play a significant role in altering the vertical sound speed profile.

2.4 Refraction

The speed of sound in the oceans varies as a function of depth, and therefore, the propagation path of the ensonifying and return acoustic wave is not a straight line. This refractive effect is usually not factored into the initial computation of the positions of the data derived from acoustic seafloor mapping systems. Hence, position errors can be introduced by the breakdown of the straight line assumption. As is shown in this section, this effect is vastly more important for multibeam than for sidescan systems.

Refraction is simply described by Snell's law, which is derived from the eikonal equation and Fermat's principle, and can be stated simply as

$$\frac{\sin\theta_1}{c_1} = \frac{\sin\theta_2}{c_2} = \text{constant},$$

as shown in Fig. 3. When c_2 is greater than c_1, the propagating ray is inclined to a shallower grazing angle; this is also known as an upward refracting environment. Conversely, when c_2 is less than c_1, downward refraction occurs as the rays tend towards the normal incident direction. Another aspect of Snell's law is that any particular ray path is uniquely described by a constant factor termed the ray parameter, $\sin\theta(z) / c(z)$.

For most of the oceans, the presence of the Sound Fixing and Ranging (SOFAR) channel means that the shallow portion of the propagation path is downward refracting, while the deeper portion is

upward refracting. If the sound speed at the seafloor exceeds that at the image platform depth, then there is an upper limit to the range that can be ensonified because the far range ray paths do not intersect the ocean floor (Fig. 4). Conversely, a downward refracting environment also imposes a practical limit to the distance that can be effectively ensonified (Fig. 5).

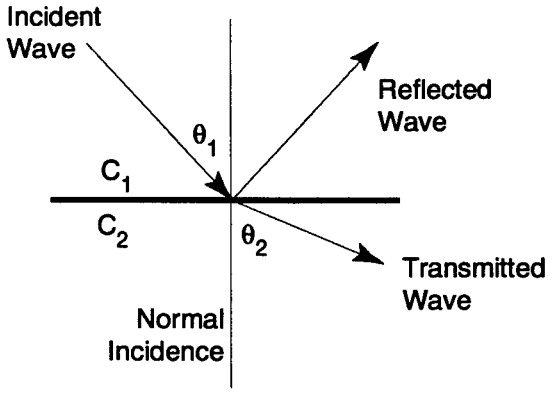

Fig. 3 — Schematic diagram of the geometry of Snell's law

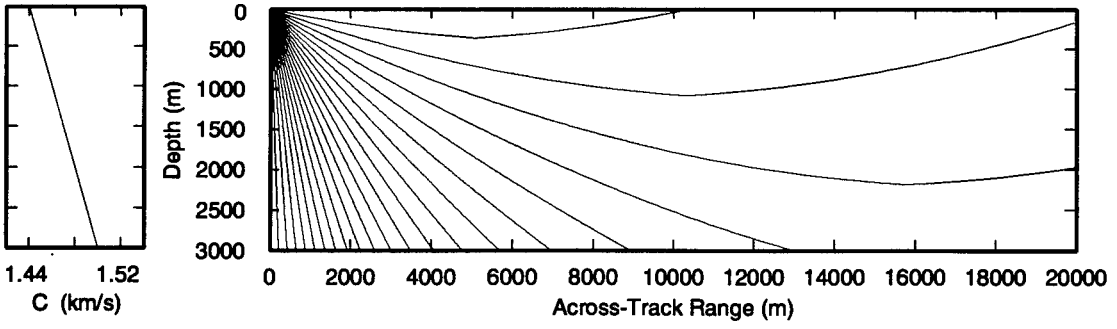

Fig. 4 — Sound speed profile (left) and ray paths (right) for an upward refracting environment where the sound speed increases with depth. Upward refraction constrains the range to which the seafloor can be ensonified. Take off angles shown are between 0 and 85 degrees with respect to the vertical direction.

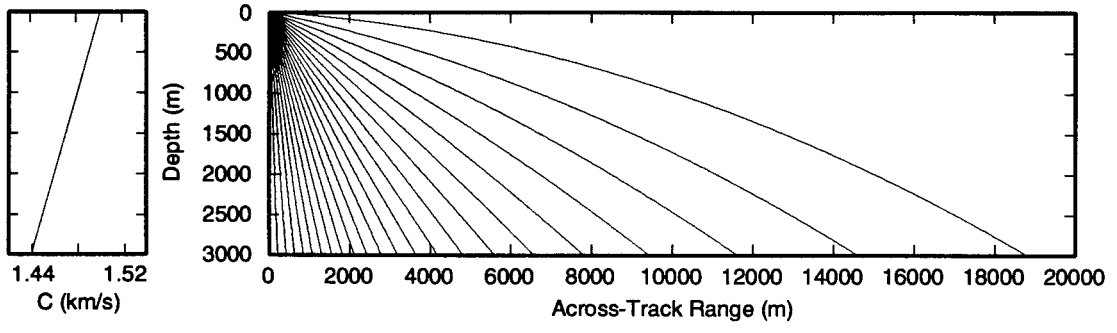

Fig. 5 — Sound speed profile (left) and ray paths (right) for a downward refracting environment where the sound speed decreases with increasing depth. Take off angles shown are between 0 and 85 degrees with respect to the vertical direction.

2.5 Transmitted Wave

When an incident compressional wave impinges on an interface, a portion of the acoustic energy may be transmitted into the next layer. Neglecting scattering for a moment, the ratio of the reflecting energy (E_{refl}) to the incident energy (E_{inc}) for the case of a normal incident angle is given by

$$\left(\frac{E_{refl}}{E_{inc}}\right)=\left(\frac{A_{refl}}{A_{inc}}\right)^2=\left(\frac{\rho_2 c_2-\rho_1 c_1}{\rho_2 c_2+\rho_1 c_1}\right)^2, \tag{7}$$

where, ρ is the density of the media, c is the sound speed, and A refers to the amplitude of the reflected (refl) and incident (inc) waves. The square root of Eq. (7) is known as the reflection coefficient.

The theoretical expressions for the reflection and transmission coefficients become more complicated at oblique incident angles. These coefficients are derived by substituting equations that describe the amplitude displacements for a propagating wave (i.e., the solution to the general wave equation) into displacement and stress-strain boundary conditions at the interface. For the case of a liquid-solid interface, the boundary conditions are that the compressional wave amplitudes and normal stresses at the interface match, and that the shear stress and displacement values go to zero in the liquid layer. The final equation depends on the densities, sound speeds, and angle of the incident wave [50].

Finally, an important factor that needs to be considered is the critical angle of incidence. Under the conditions like that found at seafloor when $c_2 > c_1$, there is an angle θ_1 such that

$$\frac{c_2}{c_1}\sin\theta_1 = 1 .$$

Beyond the critical angle, there is no simple transmitted wave into the sub-bottom. This critical angle is given by

$$\theta_c = \sin^{-1}\left(c_1 / c_2\right) .$$

The statement that there is no transmitted wave past this critical angle conveniently neglects such possible propagation effects as diffraction and Stoneley wave generation.

3. ACOUSTIC BACKSCATTERING

The reverberation caused by the interaction between ensonifying acoustic energy and the seafloor is characterized by two distinct physical processes. The first process is specular reflection that is dominant at near normal incident angles. Reflection results in a relatively strong echo return with the amplitude of the return signal controlled by the reflection coefficient of the water/rock interface (Eq. (7)). This report gives only a somewhat cursory discussion of this deterministic process.

The second process described in this report is acoustic scattering. This process is characterized by a functional relationship between the intensity of the scattered energy with the angle of ensonification, the angle of the returning acoustic wave, the roughness of the seafloor, and the material properties of the seafloor (Fig. 6). Acoustic scattering occurs at all angles of ensonification

and return. However, we are primarily concerned with the case of backscattering where the return angle is the reverse of the ensonification angle. This configuration is also called a monostatic imaging geometry.

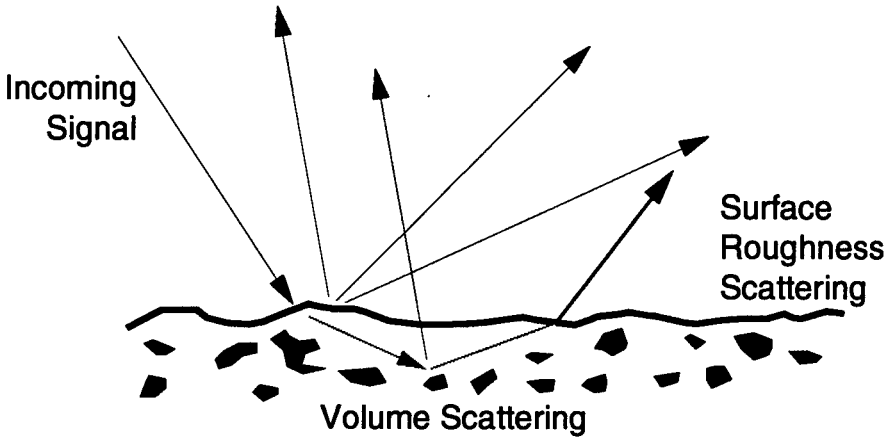

Fig. 6 — Schematic diagram indicating two sources of scattering from the seafloor. The volume scattering shown is from discrete point scatterers embedded in the sub-bottom.

3.1 Theoretical Scattering Models

Various theoretical models have been formulated to describe backscattering [51, 52]. The main derivations fall into several general classifications: 1) perturbation approach, 2) Kirchhoff approximation method, 3) multiple scattering theory, and 4) facet models. Various hybrid models have also been derived, such as the composite roughness model that combines aspects of several scattering and reflection models to obtain an integrated theory for describing acoustic returns from all angles of ensonification and return [53]. The following paragraphs provide an abbreviated summary of the main theoretical approaches used to describe scattering. While only cursory descriptions are presented, they should be sufficient to allow the reader to sound knowledgeable at cocktail parties.

3.1.1 Perturbation Models

The perturbation approximation model for rough surface scattering incorporates restrictions on the height h and gradient ∇h of the surface whereby

$$k\,|h\,| \ll 1$$

$$|\nabla h\,| \ll 1\,,$$

where k is the modulus of the wave vector of the incident wave. These assumptions essentially mean that the surface is slowly varying with no discontinuities. The total intensity field can then be approximated by an infinite series

$$\Psi(r) = \Psi^{inc}(r) + \sum_{j=0}^{\infty} \Psi_j^{sc}(r) ,$$

where $\Psi^{inc}(r)$ is the incident field, and $\Psi_j^{sc}(r)$ is the j^{th}-order term of the scattered field. This wave field approximation is subsequently truncated at some low-order derivative terms and is used as an approximation of the scattered field. For instance, one use of the perturbation approach is in the solution of the Helmholtz scattering integral that describes the scattered acoustic pressure field $\psi^{sc}(r)$ at some reference point r by

$$\psi^{sc}(r) = \frac{1}{4\pi} \int_{S_o} \left[\psi^{sc}(r_o) \frac{\partial U(R)}{\partial n} - U(R) \frac{\partial \psi^{sc}(r_o)}{\partial n} \right] dS_o \tag{8}$$

$$U(R) = \frac{\exp(ikR)}{R} ,$$

where S_o is the rough surface, r_o is the vector over this surface, n is the unit vector of the normal to the rough surface at point r_o, k is the wave number, and R is the distance from the reference point to the rough surface (Fig. 7).

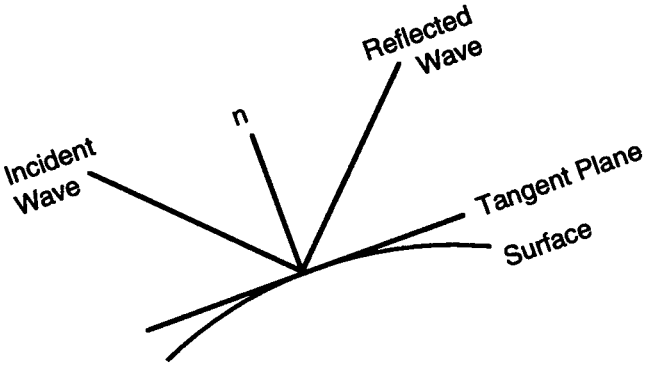

Fig. 7 — Scattering geometry for the Helmholtz/Kirchhoff formulation

Any other function that has a boundary condition equal to zero at the surface can be written as a Taylor series expansion:

$$f(x,y,z)\big|_{z=h(x,y)} = 0$$

$$f(x,y,z)\big|_{z=h(x,y)} = f(x,y,z)\big|_{z=0} + h \left.\frac{\partial f}{\partial z}\right|_{z=0} + \frac{h^2}{2} \left.\frac{\partial^2 f}{\partial z^2}\right|_{z=0} + \cdots$$

The function $f(x,y,z)$ can represent, for example, the stress components on the surface. The Taylor series is then truncated at the first or second derivative term and is substituted into the various boundary conditions that are used to solve the wave equation.

3.1.2 Kirchhoff Approximation

The Kirchhoff, or tangent plane, approximation assumes that any point on the rough surface can be approximated to be locally flat (planar). For the Kirchhoff approximation to be valid,

$$k\, a \cos^3\theta_\perp \rangle\rangle 1 ,$$

where $\theta_\perp$ is the angle of the incident wave relative to the mean plane normal direction, k is the modulus of the wave vector of the incident wave, and a is the radius of curvature of the surface. This thereby imposes a tradeoff between the curvature of the surface and the wavelength of the incoming wave. The Kirchhoff approximation differs from the perturbation method in that there is no explicit restriction on the magnitude of the surface height or gradient. However, like the perturbation approximation, the surface cannot have rapid changes in the surface height or gradient.

The Kirchhoff approximation states that the pressure field of the scattered wave and the pressure gradient of the scattered wave at the surface can by expressed simply in terms of the pressure field of the incident wave and a reflection coefficient $\Re$ where

$$\psi^{sc}(\boldsymbol{r}_o) = \Re\psi^{inc}(\boldsymbol{r}_o)$$

$$\frac{\partial\psi^{sc}(\boldsymbol{r}_o)}{\partial n} = -\Re\frac{\partial\psi^{inc}(\boldsymbol{r}_o)}{\partial n} .$$

These expressions are substituted into the Helmholtz scattering integral (Eq. (8)) to yield

$$\psi^{sc}(\boldsymbol{r}) = \frac{1}{4\pi}\int_{S_o} \Re\left[U(R)\frac{\partial\psi^{inc}(\boldsymbol{r}_o)}{\partial n} - \psi^{inc}(\boldsymbol{r}_o)\frac{\partial U(R)}{\partial n}\right] dS_o . \tag{9}$$

The scattering at point **r** is now expressed as a function of the incident wave pressure field. The solution to Eq. (9) is non-trivial and has been the topic of much theoretical development.

3.1.3 Composite Roughness Model

One model that has gained considerable acceptance is the composite roughness model that incorporates both the perturbation and Helmholtz-Kirchhoff scattering theories. In the derivation of Jackson et al. [53], the scattering strength $S(\theta)$ at some angle θ is given by

$$S(\theta) = \frac{g^2(\pi/2)}{8\pi\sin^2\theta\,\cos^2\theta}\int_0^\infty \exp(-qu^{2\alpha})\, J_o(u)\, u\, du ,$$

where $J_o(u)$ is the zero order Bessel function of the first kind:

$$q = \sin^2\theta\, \cos^{-2\alpha}\theta\, C_h^2 2^{1-2\alpha} k_\alpha^{2(1-\alpha)},$$

where $g(\pi/2)$ is the plane-wave reflection coefficient for a normal incident wave:

$$C_h^2 = \frac{2\pi\beta\,\Gamma(2-\alpha)\;2^{-2\alpha}}{\alpha(1-\alpha)\;\Gamma(1+\alpha)},$$

and where Γ is the gamma function. Parameters α and β are used to characterize the roughness of the seafloor that is assumed to be isotropic with Gaussian statistics. In this case, β is the spectral strength of the roughness and α is related to the slope of the spectrum.

In the composite roughness model, the Kirchhoff approximation, which can handle large RMS relief and slope, is used to model the backscattering caused by the long wavelength component of the seafloor. The perturbation model is then used to model the shorter wavelength component where the radii of curvature are small. At steep grazing angles (near normal incidence), the composite model is replaced by the Kirchhoff approximation.

3.2 Random Phase Scattering Model

In real world applications, it is not feasible to deterministically describe the exact distribution of scatterers on the seafloor. Instead, the microroughness of the seafloor and the distribution of scatterers are modeled by some statistical random process. The random nature of the seafloor therefore means that the coherent imaging of the acoustic scattering field is also random. This point can be better illustrated by the following example of the random phase scattering model [54].

Suppose the seafloor is characterized by a random spatial Gaussian distribution of point scatterers distributed on a flat plane (i.e., constant depth). In the random phase scattering model, the contribution from a single scatterer is characterized by a signal that has phase components that vary randomly between 0 to 2π. This signal, $S(t)$, can be written as

$$S(t) = a(t)\,\cos(\omega t) + b(t)\,\sin(\omega t)\,,$$

where the real $a(t)$ and imaginary $b(t)$ components of the signal are random functions. The amplitude (A) and phase (ϕ) components of the backscattered signal are therefore given by

$$A = \sqrt{a^2 + b^2}$$

$$\phi = \tan^{-1}(b/a)\,.$$

Since the real and imaginary components (a and b) are Gaussian, the amplitude of the signal is characterized by a Rayleigh statistical distribution. Furthermore, since a and b are random, the phase term is also random.

The coherent imaging of such a field results in the backscattered signal being characterized by random interference terms if the scattering volume is greater than the wavelength of the incoming signal. The time integrated (averaged) signal S from a series of multiple scatterers is then given by

$$S = \int_{t_1}^{t_2} [a(t)^2 + b(t)^2]dt$$

or equivalently by

$$S = \sum_{j=1}^{N} s_j \exp(i\varphi_j) ,$$

where s_j is the scattering amplitude for the scatterer at position j, ϕ_j is the random phase, and N the total number of scatterers ensonified during the time period t_1 to t_2.

3.3 Speckle

The random statistical nature of backscatter from a real seafloor results in the presence of noticeable high and low pixel values in the acoustic imagery data. This speckle is characterized by a mean intensity value, variance, and potentially other statistical parameters. It should be noted that speckle does not necessarily represent noise in the imagery data; rather, it indicates the statistical scattering characteristics of the seafloor.

The amount of speckle is highly dependent on the length of the time integration used to generate the pixel values. Long time integration yields imagery data with less speckle than is generated during a short time integration. However, this type of speckle reduction is offset by a comparable reduction in the spatial resolution of the data. Another means of reducing the amount of speckle is to perform repeat measurements with a fixed imaging platform and target, and to then take the ensemble average of these measurements. Unfortunately, acoustic remote sensing is hampered by the relative slow propagation speed of the signals and, hence, obtaining repeated measurements is not a viable option in routine survey operations. Speckle is therefore an omnipresent entity in acoustic imagery data. This then has an impact on the efficiency and effectiveness of using data compression algorithms to reduce the data storage requirements as the lack of redundancy in the data is not amenable to compression.

As a side note, speckle in optical electromagnetic scattering is not readily visible to the naked eye because we essentially record an ensemble average of the backscattered signal from a single location. High time resolution measurements using pulsed lasers have clearly demonstrated that optical backscattering is characterized by the presence of speckle and that the amplitude can be modeled by a Rayleigh distribution.

3.4 Lambertian Scattering

One of the simplest means of describing surface roughness scattering strength is by applying Lambert's rule (sometimes called Lambert's law). A Lambertian surface obeys the relationship

$$I = I_o \cos^2(\theta) , \tag{10}$$

where I_o is the backscattering strength of the surface and θ is the normal angle component of the incident wave. In general, this simple relationship is an adequate approximation for angles between 15° to 75°. A perusal of Lambert's rule indicates that scattering strength is greatest at vertical incidence and diminishes for lower grazing angles.

3.5 Volume Scattering

It is becoming more apparent that under certain conditions volume scattering in the sub-bottom contributes significantly to the strength of the backscattered return signal. This occurs mainly in areas

where the seafloor is characterized by sediment cover [55] (Fig. 6). The source of the additional backscattering is believed to be thin interbedded sediment layers [56] or embedded point scatterers within the uppermost sediments. The possible effect of volume scattering is greater for lower frequency waves as they are more susceptible to sub-bottom penetration and undergo less attenuation in the sub-bottom. Under average conditions, 10 kHz waves effectively penetrate into the sub-bottom to a depth of a few meters.

4. DATA COLLECTION SYSTEMS

Several types of sonar systems are used to collect acoustic backscatter imagery data of the seafloor. These systems include:

1. sidescan systems
2. multibeam bathymetric systems
3. synthetic aperture sonar systems
4. generic directional sonar systems

Of these types of data collection systems, the first two represent established technology that is currently operational and fairly well understood. The third, synthetic aperture sonar, is currently under development, while generic systems are mainly exploratory. This section provides an overview of the different systems, with an emphasis given to the first two types.

4.1 Sidescan Systems

Sidescan systems represent a well-established methodology used to collect acoustic backscatter imagery of the seafloor. Examples of low-frequency sidescan systems (i.e., ones that use a transmit frequency of less than 20 kHz) include SeaMARC II (Seafloor Mapping And Remote Characterization), GLORIA (Geological Long Range Inclined ASDIC), GLORI-B, SEAMAP, HAWAII MR1 (HIG Acoustic Wide Angle Imaging Instrument Model Revision 1 or Mark Ronstadt 1), TAMU^2 (Texas A&M University Towed Acoustic Mapping Unit), SYS9, and Izanagi (Table 1). All of these systems are configured in relatively large towfishes (>15 ft long) that are towed behind ships of opportunity. While these sidescan systems are operated in a similar manner, their data collection and processing schemes do vary in high correlation with the age of the system's hardware and software.

An important aspect of sidescan sonar systems is the need to have a focused ensonification of the seafloor in the across-track (i.e., perpendicular to the orientation of the towfish) horizontal direction (Fig. (8)). This controlled ensonification of the seafloor is required so that the return backscattered energy can be ascribed to be from only this area. An omni-directional acoustic source generates return signals from a wide range of directions that makes the interpretation of the imagery data difficult. Hence, in order to achieve this directional ensonification, sidescan systems use separate port and starboard side horizontal linear transducer arrays. The individual transducers within the arrays are selectively triggered using some predetermined time delay. When properly designed, this selective time-delay triggering results in a focused beam of acoustic ensonification in the horizontal across-track direction with the narrowness of the beam related to the length of the array of transducers. The vertical beam pattern for sidescan systems is generally broad to ensure the ensonification of a wide across-track section of the seafloor (Fig. 8). This maximum direction of the vertical beam pattern is inclined at some preset angle.

Table 1 — Examples of Low-Frequency Sidescan Systems

System	Manufacturer[1]	Operator[1]	Freq[2]	Comments[3]
SeaMARC II	IST	UH	11/12	(B) [57] lost 1991
SEAMAP	UH	NAVOCEANO	11/12	(B)
SEAMAP II	UH	NAVOCEANO	11/12	(B) Being built
HAWAII MR1	UH	UH	11/12	(B)
GLORIA Mk II	IOS	IOS	6.2/6.7	[18, 19]
GLORI-B	IOS	IOS	6.2/6.7	(B) [33] Improved GLORIA Mk III
Izanagi	Honeywell	ORI, Univ. of Tokyo	11/12	(B)
SYS9	SSI	SSI / IFREMER	9	(B) [58]
MR1	UH	UH	11/12	(B)
Okean	Unknown	CGGE, Russia	9/10	[59]
TAMU[2]	IST / Honeywell	Texas A&M University C & C Technologies Inc.	11/12 72	(B) [60] Multispectral

1. IST —International Submarine Technology; UH — University of Hawaii; NAVOCEANO — Naval Oceanographic Office; IOS — Institute for Ocean Sciences (UK); ORI — Ocean Research Institute; SSI — Seafloor Surveys, Inc.; IFREMER — Institut Francais de Reçherche pour l'Exploitation de la Mer; CGGE — Central Geology & Geophysics Expedition
2. Frequencies listed port/starboard in units of kHz.
3. (B) in the comments denotes systems capable of collecting bathymetric data

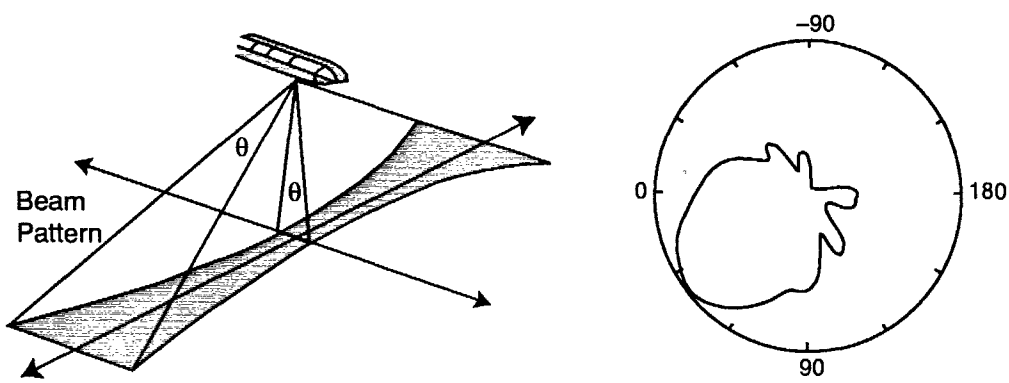

Fig. 8 — Illustration showing the narrow horizontal (left) and vertical transmit beams (right) from a sidescan system. The horizontal beamwidth of this system is θ and is usually 1° to 3°. If the seafloor is relatively flat, then a wider along-track area is ensonified at the outer edges of the swath. On the right is the measured SeaMARC II port side vertical transmit beam pattern. Note the presence of sidelobes in the nadir (90°), upwards (–90°), and starboard (180°) directions.

The returned acoustic signals from the seafloor are subsequently recorded by a row of receivers; in many cases, these receivers are the same transducers used to transmit the outgoing ping. In general, the receive broadside beam is computed with the horizontal beamwidth usually the same as that of the

transmit beam. Given some knowledge of the height of the towfish over the seafloor (first-bottom detect time), time segments of the signal are subsequently averaged to yield across-track intensity values as a function of across-track range.

Another design component of many sidescan systems is the use of two different transmit frequencies for the port and starboard transducers; for instance, SEAMAP transmits at 11 kHz (port) and 12 kHz (starboard). This difference is to compensate for the irregular transmit and receive beam pattern whereby signals from one side of the imaging platform can be received by the arrays on the opposite side. If the bandwidth of the transmitted pulse is small enough, then there is no overlap in the frequency content of the port and starboard signals. Sections 6.1 and 8.1 discuss the important role that suppression of these unwanted signals can play in sidescan systems, and in the elimination of crosstalk artifacts.

4.1.1 Sidescan Survey Operations

Dedicated sidescan systems are housed in specialized tow-bodies that are towed behind a ship or boat (Fig. 9). These tow-bodies are designed to be appropriately hydrodynamic efficient while also housing the arrays, requisite electronics, various additional sensors (e.g., motion sensors), and flotation units. As described Section 5.2, the size (and, hence, the weight in air) of the towfish is more or less determined by the transmit frequency of the system.

Large low-frequency systems are usually housed in near neutrally buoyant towfishes that are towed at speeds up to 10 knots. In order to position the towfish at a sufficient depth, which is ideally below the surface thermocline, a heavy (~ 1 ton) depressor weight is placed between the main towing cable and a neutrally buoyant umbilical line. The depressor weight also serves to dampen the irregular stresses imparted by the towing ship that are created by ship's pitching motion. It is has also

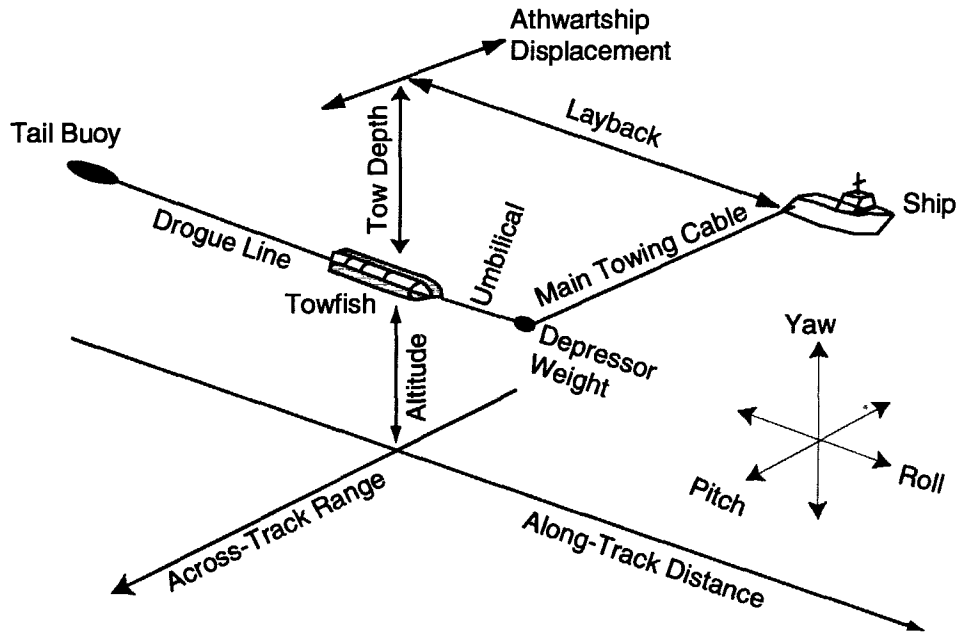

Fig. 9 — Schematic diagram showing a typical deployment geometry of a towed sidescan system. The pitch, roll, and yaw diagram indicates the axis of rotation that describes the motions.

been theorized that much of the platform towing stability is primarily due to the use of a neutrally buoyant towfish and umbilical line [61]. Additionally, some systems (e.g., SEAMAP and MR1) use a drogue line that is deployed behind the towfish. This drogue line essentially acts as a sea anchor that also helps to stabilize the towfish. In practice, pitch and yaw motions of less than 1° are desirable.

High-frequency sidescan systems are housed in smaller assemblages that are towed behind or alongside a ship or boat. In standard operations, there is no drogue line nor depressor weight deployed. Instead, platform stability is predicated on a combination of the hydrodynamic efficiency of the towfish, lower towing speeds, use of stabilizing fins, and towing platform stability. If the higher frequency system needs to positioned close to the seafloor, then obstacle avoidance maneuvering of the towfish can become a source of platform instability.

The standard mode of survey operations of an acoustic backscatter imaging system is to run a series of parallel lines over the area of interest. The maximum spacing between adjacent lines is determined by the effective swath width of the system, which is controlled by the transmit frequency. Closer line spacing, which results in significant coverage overlap, is sometimes desirable because it generates multiple look direction acoustic imagery in the regions of overlap. A survey that incorporates parallel lines is called "mowing the lawn."

Another consideration that controls the layout of survey lines is the general orientation of the topographic features in the region. Due to the ensonification angle dependency of backscatter, it has been empirically derived that it is desirable to run the survey lines at an oblique angle to the general trend of these features. When a particular feature that has bathymetric relief is crossed over by the towfish, the received backscatter signal changes from a strong to a weak return (or vice versa) (Fig. 10). Conversely, the absence of this polarity reversal would then indicate that the feature represented

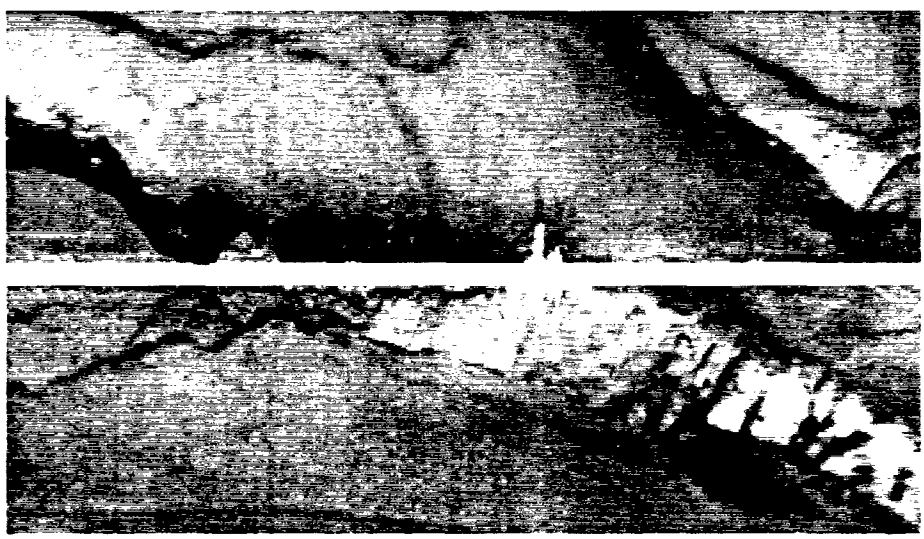

Fig. 10 — This sidescan image demonstrates the change in received backscatter strength when crossing over a feature with bathymetric relief. The strong signals (dark) from the fault scarp on the upper left part of the image indicate a facing bathymetric slope. This strong return becomes a weaker return (light) in the lower right portion of the image as the fault scarp is ensonified in the downslope direction. The horizontal white line in the middle is the nadir region under the towfish. Crosstalk is present on the left-hand side of the image.

a material property difference when compared to the surrounding seafloor. Overlapping swath coverage characterized by opposite ensonification directions can also provide this type of information (Fig. 11). It is also well known that linear features aligned perpendicular to the track of the mapping system are poorly imaged. In some cases, negligible return signals are recorded, while in other instances, the features themselves appear distorted.

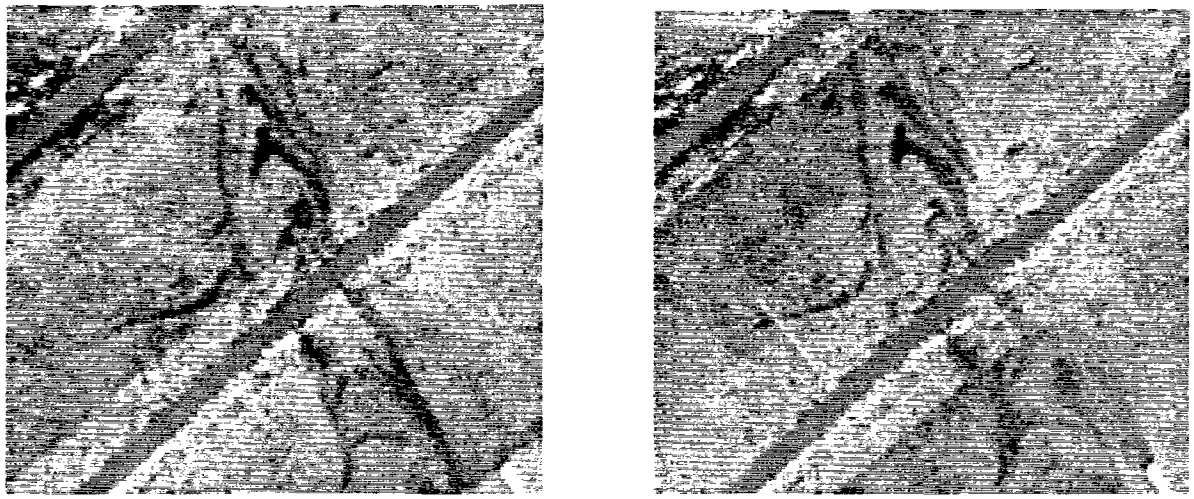

Fig. 11 — Sidescan mosaics illustrating the use of multiple look directions obtained from overlapping swath coverage. The mosaic on the left is basically one where the ensonification direction is from the upper left, while the mosaic on the right is from the lower right. The swirly feature in the two mosaics looks extremely similar with no polarity reversal. This feature represents some type of material property difference compared to the surrounding seafloor. The straight gray lines are filled in data gaps corresponding to the track of the instrument (SeaMARC II).

4.1.2 Dual-Frequency Sidescan Systems

A special type of sidescan system is one that uses two sets of arrays that transmit at distinctly different frequencies (Fig. 12). These multispectral remote sensing tools are similar in principle to multi-frequency radar or microwave imaging systems. One should note that there is one major difference between electromagnetic and acoustic multispectral imaging: acoustic propagation is characterized by a strong frequency dependent attenuation. This limits the effective imaging range of the sidescan system to the lesser range of the higher frequency used.

Below 100 kHz, the degree of sub-bottom penetration can vary substantially as a function of transmit frequency. This latter effect is important because the amplitude of the transmitted wave into the sub-bottom is inversely correlated with the amplitude of the reflected signal and also the amount of surface scattering. For a relatively transparent seafloor, both the reflected and backscattered signal are essentially weak. If thin horizontal layering or embedded volume scatterers are present in the uppermost layers of the sub-bottom, then these return relatively strong backscattering signals. The end result is a relatively weak signal recorded on the high frequency image, and a relatively strong signal on the low-frequency image.

The use of a multifrequency system is also an advantage in target search and identification missions. For these applications, the lower frequency with its inherently greater imaging range is used

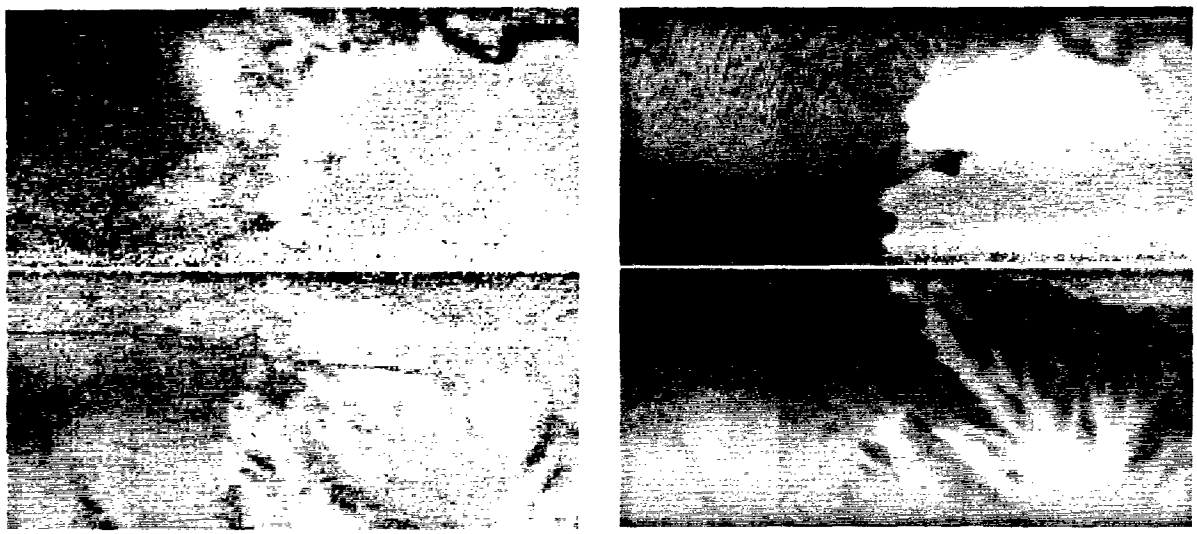

Fig. 12 — Example of multispectral sidescan data. On the left is backscatter imagery data collected from the 11/12 kHz arrays of TAMU[2] and on the right is the coregistered 72 kHz image. Shown is a track plot with the towfish moving from left to right; the swath width is 500 m. The weak (light) sediment flow in the 70 kHz image is characterized with by a relative sharp boundary compared to that of the 11/12 kHz image. The additional weak scattering areas in the left-hand image indicates an earlier depositional flow(s) that is acoustically transparent to 11/12 kHz signals but not at 72 kHz.

to perform an area-wide search for targets. The higher frequency system is then used to better identify the located targets. The advantage of a dual frequency system is that the instrument platforms do not need to be recovered and redeployed in order to change the imaging resolution.

4.1.3 Bathymetric Sidescan Systems

Starting with SeaMARC II, some low-frequency sidescan systems have been designed and built with two parallel transducer arrays situated longitudinally on each side of the tow-body (Fig. 13). These two linear arrays are spatially offset at some prescribed distance that is ideally half the wavelength of the transmit frequency. With the assumption that the signals received at the two separate arrays are the same, then the measured time delay, or equivalently, the phase lag of these two signals is used to compute what is termed the acoustic incident angle of arrival. This acoustic angle is subsequently converted to the true geometric incident angle which when combined with the slant range is then used to compute the across-track seafloor bathymetry profile.

In practice, however, the computed acoustic angle is not usually the same as the geometric angle of arrival. Furthermore, it is currently not practical to theoretically compute the proper conversion function. Hence, empirical lookup tables are computed and are subsequently applied.

Bathymetric sidescan systems are currently capable of measuring the topography of the seafloor to a precision of approximately 3% of the water depth. An inaccurate empirical lookup table can also contribute to errors in the depth values and hence sidescan system derived bathymetry is rather noisy when compared to multibeam systems.

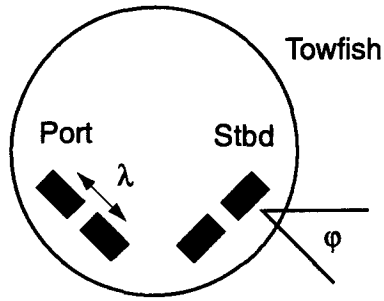

Fig. 13 — Schematic cross-section of a dual array bathymetric sidescan system (e.g., SeaMARC II). The shaded boxes are the individual arrays. The angle φ is the inclination of the array; this angle is also called the boresight of the arrays.

4.2 Bathymetric Multibeam Systems

Advances in computer hardware and software during the past decade have made practical the collection of acoustic backscatter imagery using multibeam bathymetric systems. For instance, SeaBeam2000, SASS Phase IV, Simrad12A, and HYDROSWEEP are examples of multibeam systems that are currently capable of generating backscatter imagery data (Table 2). As these multibeam systems are becoming increasingly prevalent, the amount of available acoustic imagery data will correspondingly increase.

The orientation of the transmit arrays of a multibeam system is like those of sidescan system in that the transducers are horizontal linear arrays configured to produce a narrow across-track region of ensonification. The vast majority of multibeam systems use only a single linear array (Simrad12A is an exception to this rule) compared to a sidescan's port and starboard transducers. The transmit vertical beam pattern has a wide main beam pattern that is directed in the vertical direction. The use of a single array also means that a multibeam system cannot differentiate between port and starboard side arrivals by the frequency difference of the return signals.

Multibeam systems receive the return signals using a separate longitudinal array that is mounted in the athwartship direction. This array is used to generate individual focused beams that are narrow in the vertical plane and broad in the fore-aft direction (Fig. 14). The slant range time is the peak amplitude arrival recorded on each beam. Depth measurements are then computed using this slant range time, an assumed sound speed, and the inclination angle of the beam. The spatial resolution of multibeam data is controlled by the pulsewidth of the transmitted signal, the horizontal transmit beam pattern, the receiver beamwidths, and by the along-track spacing between pings.

A difference between hull-mounted multibeam and towed sidescan systems is how they are operated. Towed systems need to be deployed and recovered, which sometimes imposes operating limitations during high sea state conditions. Conversely, a towed sidescan system, once deployed, is a more stable platform than the towing ship in high sea states. Experience has shown that in rough seas, the pitching motion of the towing platform can increase the pitching motion of the towfish. However, this effect can be greatly diminished by simply reducing the towing speed; this is also desirable if you happen to be onboard the ship at that time. Finally, a major difference between a hull mounted and a towed system is that it much more likely to lose a towed system (e.g., SeaMARC II).

Table 2 — Examples of Low-Frequency Multibeam Systems

Systems	Manufacturer	Ship	Freq.	Comments
HYDROSWEEP	Krupp Atlas	R/V *Ewing* R/V *Thompson*	16 kHz	[62, 63]
SASS Phase IV	SeaBeam	USNS *Maury* USNS *Tanner* USNS *Wyman*	12 kHz	[42]
Simrad12A Simrad EM12	Simrad	USNS *Hensen* USNS *Bowditch* USNS *Sumner* USNS *Pathfinder* R/V *R'Atalante* (France)	12 kHz	[41]
SeaBeam2000 SeaBeam2100	SeaBeam	R/V *Knorr* R/V *Revelle* R/V *Melville* R/V *Nathaniel Palmer* *R/V Atlantis* R/V *Hae Yang 2000* (ROK) R/V *Onnuri* (ROK) R/V *Dayang Yi Hao* (PRC) R/V *Hai-Yang-4* (PRC) R/V *Meiyo* (Japan) R/V *Kaiyo* (Japan)	12 kHz	[64]

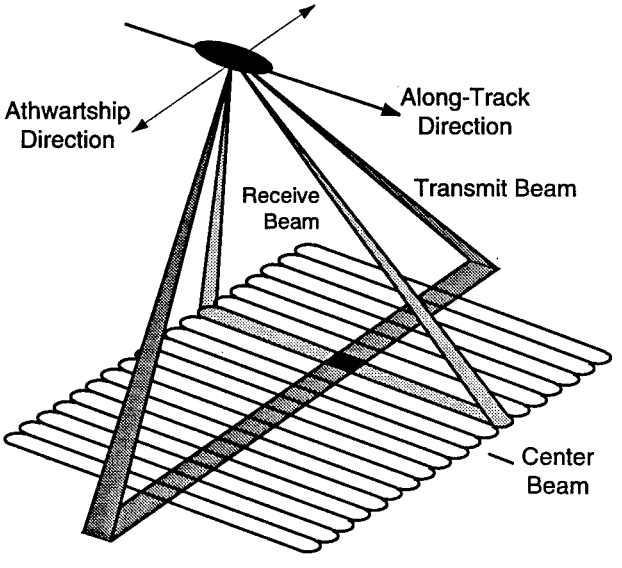

Fig. 14 — Transmit and receive beam pattern of a multibeam system. The intersection of the two sets of beam patterns determines the position of the data (black cell).

4.3 Synthetic Aperture Sonar (SAS) Systems

An emerging technology in ocean mapping is the development of synthetic aperture sonar systems capable of collecting acoustic backscatter imagery of the seafloor [65-67]. This advance methodology represents a means of obtaining acoustic imagery with a higher azimuthal resolution than that collected using a standard sidescan system. And while synthetic aperture radar is a well established tool, SAS is not, due to implementation problems caused by disturbances such as Doppler effect, propagation medium variability, reverberation, noise, and, platform instability.

In a SAS imaging system, a wide area of the seafloor on only one side of the instrument is ensonified by the transmitted pulse. As opposed to conventional sidescan systems, SAS uses the received signals recorded from several pings (Fig. 15). These received signals are subsequently beamformed to generate a wide along- and across-track backscatter image of the seafloor. The maximum length of the aperture is determined by the horizontal width of the transmitted beam; the longer the aperture, the better the azimuthal resolution.

A major limitation of SAS is the requirement that the position and orientation of the receiving arrays be accurately known to a resolution of less than the wavelength of the transmitted signal. Furthermore, the along-track spacing of the successive pings needs to be relatively close, also on the order of half a wavelength. One manner of establishing this ping-to-ping coherence is to use a fast ping repetition rate. However, the relatively slow speed of sound in water, compared to the speed of light for SAR, imposes the requirement of a slow towing speed or a reduction in the effective swath width of coverage.

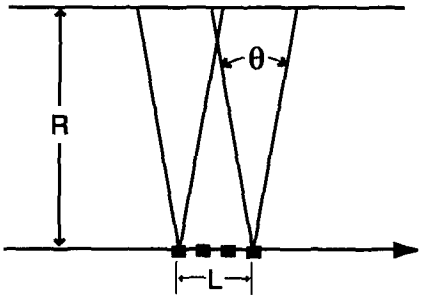

Fig. 15 — The geometry of a synthetic aperture sonar is depicted. L is the effective length of the aperture, R is the across track range, and θ is the transmit beamwidth. The black boxes indicate the positions of the sensor at the ping transmit time.

4.4 Generic Directional Sonar Systems

Any active sonar system capable of producing directional beamformed data can be modified to collect acoustic imagery data [68]. The data from such hybrid systems will naturally vary in terms of the quality and also the complexity of the imagery. These types of systems are not covered in this report.

5. SYSTEM PARAMETERS

Several system parameters determine the capabilities of a sidescan imaging system. These parameters may be fixed during the design and construction of the sidescan system, or they may be changed by the user to optimize system performance during a survey. Knowledge of these parameters is vital to the proper collection, interpretation, and analysis of the acoustic imagery data.

5.1 Transmit Frequency

The most important characteristic of an acoustic sidescan or multibeam system is the transmit frequency. The choice of a particular frequency is determined by the desired effective imaging range of the sonar device and is selected given the known frequency-dependent attenuation properties of the oceans. Once chosen, the transmit frequency then influences the design and construction of the imaging platform, the mode of survey operation, and the functionality of a particular system.

As described Section 4.1, a relatively narrow horizontal athwartship ensonification beam is highly desired. A narrow beam, usually 1° to 2° wide, is generated by the selective triggering of the individual transducers that comprise a horizontal line array. The length of this transmit array, as measured in the number of wavelengths, essentially controls the beamwidth; i.e., longer arrays produce narrower beams. Hence, low frequency systems require longer (and heavier) arrays, longer tow bodies, and additional flotation units, that in turn contribute to how survey operations are conducted. The transmit frequency also determines the amount of sub-bottom penetration of the ensonifying wave. The presence of volume scattering in the sub-bottom then affects the strength of the return signal.

5.2 Transmit Beam Pattern

Sidescan and multibeam imaging systems are designed to preferentially ensonify only a predetermined section of the seafloor (Fig. 8). This is highly desirable as the received backscattering energy can then be assumed to have originated solely from this ensonified region. The use of an omnidirectional source would yield return signals from a multitude of areas that would obviously make the interpretation of the backscattered data more difficult.

A narrow horizontal beam is generated by using a linear series of transducers that can be triggered individually according to some precomputed time delay sequence; in many cases, all the transducer elements are triggered simultaneously. The width of the transmit beam pattern is controlled by the length of the array, the number of transducers used, and the directionality of the individual transducers. Beam steering [69] and shading are other techniques that can be used.

For simplicity, consider the simple case of a linear horizontal array composed of a continuum of infinitely small transducers. For the solution of the transmitted signal in the far field (i.e., plane waves), the contribution of a transducer offset from the reference center element is given by

$$S(t,\psi) = \exp[i2\pi f(t+\Delta t)], \tag{11}$$

where f is the frequency, and

$$\Delta t = \sin(\psi)\, x / c, \tag{12}$$

where c is the sound speed ($c = f\lambda$), x is the position along the array, and ψ is the angle shown in Fig. 16. Substituting Eq. (12) into Eq. (11) yields (neglecting the time dependence),

$$S(\psi) = \exp\left[\frac{i2\pi}{\lambda} x \sin\psi\right]. \tag{13}$$

Integrating over L, the length of the array, yields

$$S(\psi) = \int_{-L/2}^{L/2} \exp\left[\frac{i2\pi}{\lambda} x \sin\psi\right] dx \tag{14}$$

$$S(\psi) = \frac{\sin\left[\frac{\pi L}{\lambda}\sin\psi\right]}{\frac{\pi L}{\lambda}\sin\psi}, \tag{15}$$

which is the well known sinc function. Keeping in mind that intensity is the square of the amplitude function (Eq. (15)), and that $S(0) = 1$, one can then compute ψ_o, the –3 dB angle (in degrees) by

$$\sin(\psi_o) = 25.3\ (\lambda / L)$$

$$\psi_o = 25.3\ (\lambda / L), \tag{16}$$

when $\lambda \langle\langle L$. Equation (16) indicates that the generation of a narrow transmit beam requires a longer array, with the length dependent on the frequency of the transmitted signal. Hence, lower frequency (i.e., longer wavelength) systems require longer arrays than higher frequency systems.

The directionality of the individual transducers can also be included in this formulation by including the transducer response function into Eqs. (13) and Eq. (14). The integral in Eq. (14) can also be changed to the appropriate summations to model the more realistic case of discrete transducer elements.

The finite beamwidth of the transmitted signal means that a wider section of seafloor is ensonified on the outer edge as opposed to the inner edge of the swath. If the beam patterns from successive pings overlap, there is an apparent stretching of features in the along-track direction. This stretching is more pronounced for features on the outer edge of the swath imagery (Fig. 17). Corrections in the form of a spatial deconvolution of the transmit beam pattern with the image can be performed [70], but this is rarely done. Also note that generating mosaicked images of a survey characterized by a

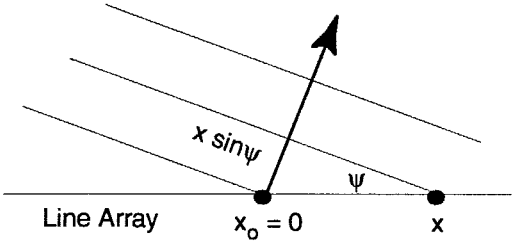

Fig. 16 — Geometry for Eq. (12)

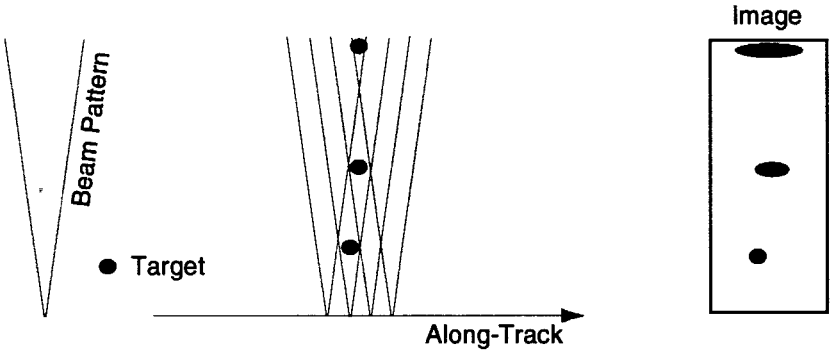

Fig. 17 — Stretching of features caused by the finite beamwidth of the imaging system. The round targets shown in the middle figure are ensonified by multiple pings. The figure on the right is a schematic of how the targets would appear in the resultant imagery.

large amount of spatial overlap between the tracks can produce apparent navigation mismatches because of stretching.

5.3 Received Beam Pattern

Sidescan systems generally perform beamforming of the received signal by the generation of the broadside beam. This is done by summing the arrivals at the individual transducer elements using a zero time delay factor for each element. If the image platform is stable, the transmitted and receive beam patterns are essentially the same in the horizontal plane (neglecting forward movement of the platform). Conversely, misalignment (pitch or yaw) of the towfish during the transmit phase or receive phase generally results in the mislocation of the imagery data and low amplitude signals.

5.4 Pulse Width

The pulse width is the time duration or, equivalently, the number of wavelengths of a transmitted acoustic ping. The amount of energy that is transmitted by a single ping is then determined by the time integrated intensity of the outgoing waveform. Hence, increasing the pulse width increases the amount of transmitted energy.

On the other hand, the pulse width, or more correctly the shape of the envelope of the transmitted pulse, controls the across-track spatial resolution of the acoustic imagery data. For instance, consider a received signal consisting of returns from two discrete sources. These signals are given by their amplitude envelopes where [71]

$$\psi_r(t) = \psi_1(t) + \psi_2(t) = a\ \psi(t - t_1) + b\ \psi(t - t_2)\ . \tag{17}$$

If the transmitted signal is undistorted on return, then the best value for the time of the return signal can be obtained by finding the value of t that minimizes the square of some error function ε:

$$\varepsilon^2(\tau) = \int_{-\infty}^{\infty} \left[\psi(t-\tau) - \psi_r(t)\right]^2 dt\ . \tag{18}$$

Substituting Eq. (18) into Eq. (17) eventually yields

$$\varepsilon^2(\tau) = a\int_{-\infty}^{\infty} \psi(t-t_1)\,\psi(t-\tau)\;dt + b\int_{-\infty}^{\infty} \psi(t-t_2)\,\psi(t-\tau)\;dt$$

and

$$\varepsilon^2(t) = \text{constant} - 2\ \text{Re}\ [\ a\,\Re_\psi(\tau - t_1) + b\,\Re_\psi(\tau - t_2)\ ]\ , \tag{19}$$

where $\Re_\psi(\tau - t_n)$ is the autocorrelation function of the signal shifted to time t_n , and Re indicates the real components. It is readily apparent that the time that minimizes $\varepsilon^2(\tau)$ is either t_1 or t_2 (Fig. 18). However, another time can also be found that minimizes this function if the two autocorrelation functions overlap significantly. Hence, it is apparent that the resolution of the signal is given be the width and shape of the autocorrelation function.

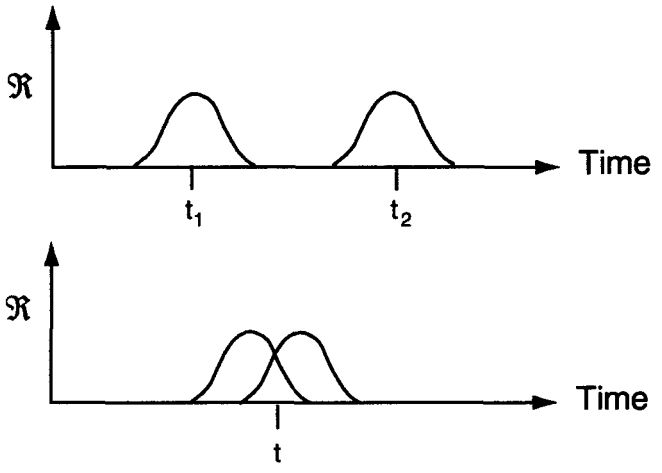

Fig. 18 — Diagram showing autocorrelation functions of two received signals. In the top figure, the correlation functions are separated and there are two clear solutions to Eq. (19). In the bottom figure, the autocorrelation functions overlap, and a third possible solution exists.

Another means of visualizing the effect that the pulse length has on the spatial resolution of the data is illustrated in Fig. 19. In this diagram, a transmitted pulse is shown intersecting a portion of the seafloor with the two arcs representing the start and end times of the pulse. Individual objects within the ensonified region are indistinguishable.

Given the normal incident angle θ, the distance from x_1 to x_2 is given by (neglecting the curvature of the wave front)

$$\Delta x = x_2 - x_1 \approx c\,\Delta t\,/\,\sin(\,\theta\,)\ , \tag{20}$$

where Δt is the pulse duration time. Therefore, as θ increases (i.e., increasing across-track range), the spatial resolution increases since Δx decreases. Furthermore, at the normal incident angle, the spatial resolution is extremely poor as Δx becomes infinite.

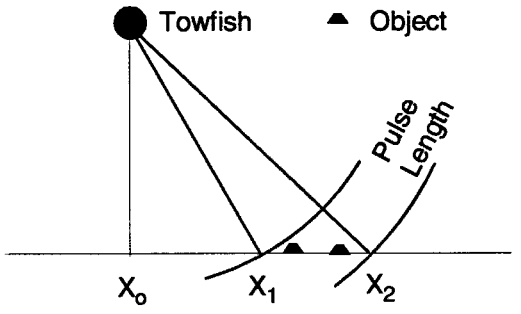

Fig. 19 — Geometry of intersection of the pulse length with the seafloor

5.5 Transmit Power

The transmit power (part of the source level (*SL*) in Eq. (1)) of an acoustic imaging system obviously directly influences the return strength of the received backscattered signal. It is also controls the maximum across-track distance that a system can effectively ensonify as it counteracts transmission loss due to geometric spreading and attenuation.

Many manufacturers of seafloor mapping systems state a particular maximum *SL* in dB's without specifying what the reference values are or what type of dB is being denoted. For instance, it should be rather surprising that the 12 kHz SEAMAP has a ~215 dB *SL*, while several systems over 100 kHz list an *SL* of around 230 dB. This discrepancy is caused by using a different definition of dB; e.g., peak-to-peak values vs the true dB defined in Section 2.1. In the peak-to-peak definition, the instantaneous pressure corresponding to the maximum amplitude transmitted wave is used (Eq. (2)) instead of the average pressure value of a continuous wave. One simple correction factor that can be applied is to consider the pulse length duration Δt with respect to a reference ping of one second. The reduction in dB is then 10 log(Δt), where Δt is in units of seconds.

The output power level is system-dependent and is determined by the applied electrical load and the transducers' effectiveness in converting this to acoustic energy. Inconsistent conversion of electrical to acoustic energy is sometimes a problem with some acoustic imaging systems. This inconsistency results in an interleaving of stronger and weaker ping returns that are displayed as "stripes" in the data.

The high wattage requirements of low-frequency systems (e.g., SEAMAP transducers can be driven to 10 kW) necessitates the use of storage capacitors. The charging time of these capacitors and the discharge levels essentially control what the fastest ping rate of a system can be. On the other hand, high frequency imaging systems require less wattage and are usually fired by applying a direct electrical load from a standard power generator; high pulse repetition rates are then possible. To illustrate this last point, consider a 230 dB 100 kHz source (peak-to-peak dB) with a pulse length of 0.1 μs and a ping rate of 1 s; converting to true dB yields a value of 190 dB. Using Eq. (3) we then find that 100 W is required for a perfect conversion of electrical to acoustic energy.

5.6 Ping Rate

The ping rate is defined as the time between successive transmitted pulses, and is a user-controlled parameter of an imaging system. The chosen ping rate is usually selected to be slightly greater than

the two-way slant range time of the propagation path to the outermost edge of the swath. The ping rate is, therefore, dependent on the altitude of the imaging platform over the seafloor and the swath width. It can also be limited in low-frequency systems by the charging time of the storage capacitors used to trigger the transducers.

The contribution of the ping rate to the spatial resolution of the data depends on the horizontal beamwidth of the imaging system. A fast ping rate (or slow platform speed) leads to a higher spatial resolution but not necessarily a significant one (Fig. 20). If the horizontal beams of successive pings greatly overlap, then the increase in spatial resolution is minimal because the information collected is redundant. Conversely, if the ping rate is too slow, then spatial aliasing may occur.

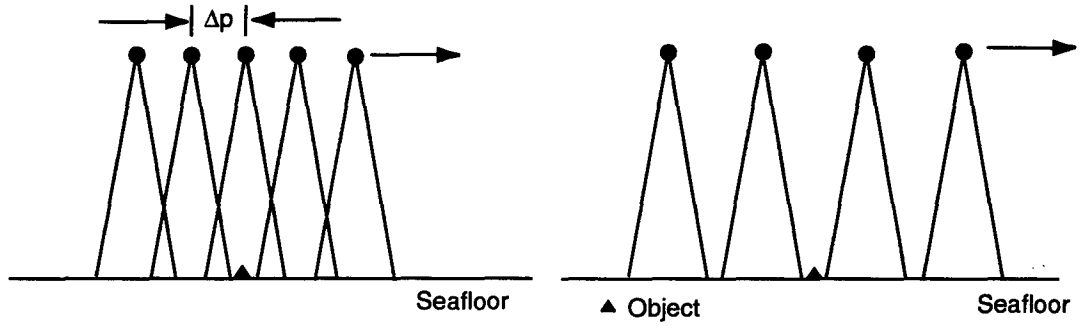

Fig. 20 — Tradeoff between the horizontal beam pattern and the ping rate. The figure on the left shows the maximum spacing between pings Δp required to resolve an isolated feature on the seafloor. The figure on the right is an example of when the ping spacing is too wide. The object on the right can be imaged if the beam pattern was greater or if Δp was reduced.

6. PROCESSING METHODOLOGY

The post-processing of sidescan imagery data is similarly performed by all major data collection and processing organizations [72-88]. This uniformity of methodology represents the commonality of the corrections required to clean up acoustic imagery data collected from a host of instrumentation. As such, the basic level processing steps outlined in this section represent a rather mature technology.

Historically, the effective processing of acoustic imagery data was primarily hindered by limited computer technology (i.e., processing speed and data storage capacity). Acoustic imagery data are approximately one to two orders of magnitude more voluminous than multibeam data sets. Since processing speed and data storage capacity double every 1-1/2 years, it would take approximately 8 years to achieve this one to two order of magnitude advance in computer technology. A perusal of the scientific and engineering literature qualitatively indicates a similar time lag between the practical digital processing of multibeam and sidescan data.

6.1 Bandwidth / Quadrature Sampling

Many sidescan systems transmit a single frequency continuous wave (CW) signal characterized by a carrier frequency f_c, where the signal $s(t)$ is given by

$$s(t) = E(t)\cos\left[2\pi f_c t + \phi(t)\right],$$

where $\phi(t)$ is the phase of the signal, and $E(t)$ is the amplitude envelope of the outgoing wave. If the received signal has a form similar to that of the transmitted pulse, it is only necessary to consider the base-banded quadrature sample of the signal (when bandwidth $<< f_c$),

$$s(t) = I(t)\cos(2\pi f_c t) - Q(t)\sin(2\pi f_c t), \tag{21}$$

$$I(t) = E(t)\cos(f(t)) \quad \text{(in-phase component)},$$

and

$$Q(t) = E(t)\sin(f(t)) \quad \text{(quadrature component)},$$

where I and Q are the in-phase and quadrature components. The complex envelope $u(t)$ of $s(t)$ is given by

$$u(t) = I(t) + i\,Q(t)$$

$$s(t) = \mathrm{Re}\,[\,u(t)\exp(i\,2\pi f_c t)\,], \tag{22}$$

where Re[ ] means the real component. One advantageous property of a bandlimited signal is that it can be represented by an equivalent frequency-shifted lowpass signal centered at zero frequency. This characteristic greatly reduces the data storage and data transmission requirements without a loss in information content.

For a single-frequency CW sidescan system, the effective bandwidth is related to the inverse of the pulse length of the transmitted signal. Consider the case of a single-frequency (ω) cosine signal with a box car amplitude envelope of duration t_p seconds:

$$s(t) = H(t)\cos(\omega t), \tag{23}$$

where $H(t) = 1$, for $\{-t_p/2 < t < t_p/2\}$, and is zero elsewhere. The Fourier transform of this signal is the sinc function:

$$S(\omega) = t_p \frac{\sin(\omega t_p/2)}{\omega t_p/2}. \tag{24}$$

One could then select the first zero-crossing ($1 / t_p$) as being representative of the effective bandwidth, which leads to the relationship

$$\text{bandwidth} = -1/t_p < f < 1/t_p. \tag{25}$$

Equation (25) results in the realization that shorter pulse lengths have a greater frequency bandwidth than do longer pulses.

6.2 Generation of Across-track Pixel Values

The methodology for generating across-track pixels of ping acoustic imagery data differs between multibeam and sidescan systems, with these differences playing a significant role in position accuracy.

6.2.1 Sidescan System Pixel Generation

The time-series signals of the backscattered acoustic intensities are measured by the towfish transducers, converted to digital form, and are time-averaged to generate across-track pixel values. The time function used in this averaging is adjusted for each ping in order to generate evenly spaced across-track pixels. In the simplest form, an assumption of a flat seafloor is used (Fig. 21) whereby the intensity I at an across-track position x is given by

$$I(x) = \int_{t_1}^{t_2} I(t)\, dt \tag{26}$$

$$t_1 = \sqrt{x_1^2 + z^2}/c \qquad t_2 = \sqrt{x_2^2 + z^2}/c$$

where z is the towfish attitude over the bottom, x is the across-track range from the nadir, and c is the sound speed. The distance $x_2 - x_1$ is the spacing between pixels. It is obvious that if z is incorrect, or if the seafloor is not flat, then the across-track positions are correspondingly inaccurate.

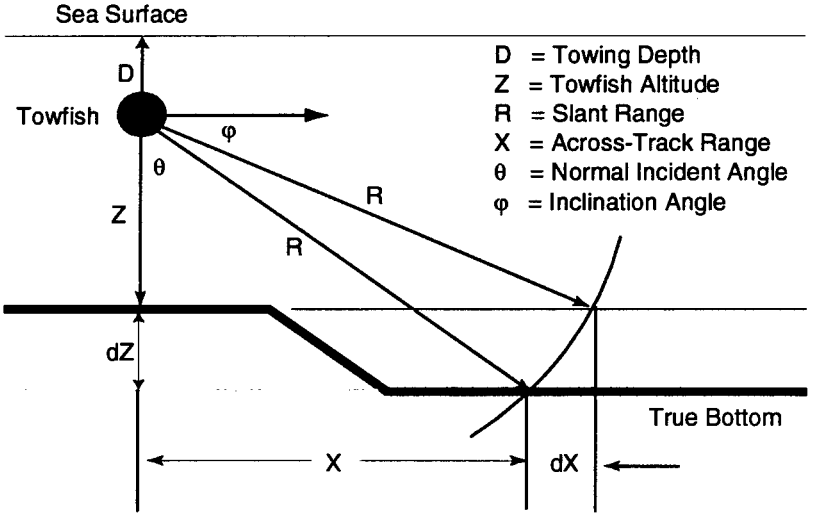

Fig. 21 — Geometry used to compute the across-track pixel location for a sidescan system. Shown is the difference in position between the flat-bottom assumption and the true seafloor depth.

6.2.2 Sidescan Repixelling

It is possible to recompute the sidescan imagery pixel values for the case of a non-flatbottom geometry [89-91]. This naturally requires the *a priori* knowledge of the seafloor bathymetry in the

survey area, and the best estimate of the sidescan system navigation within the region. Repixelling can be performed on the raw acoustic time-series data recorded by the arrays, or can be performed after pixel generation using the flat-bottom assumption. We discuss here the latter case.

The methodology for repixelling is fairly straightforward. The first step is to compute the across-track bathymetric profile for an individual sidescan ping. This can be accomplished by projecting the across-track sidescan swath coverage onto a gridded bathymetric data set, and by subsequent sampling of the bathymetric data values (Fig. 22). The new repixelled sidescan data are then generated by resampling the original flat-bottom data using travel times computed from the real across-track depths.

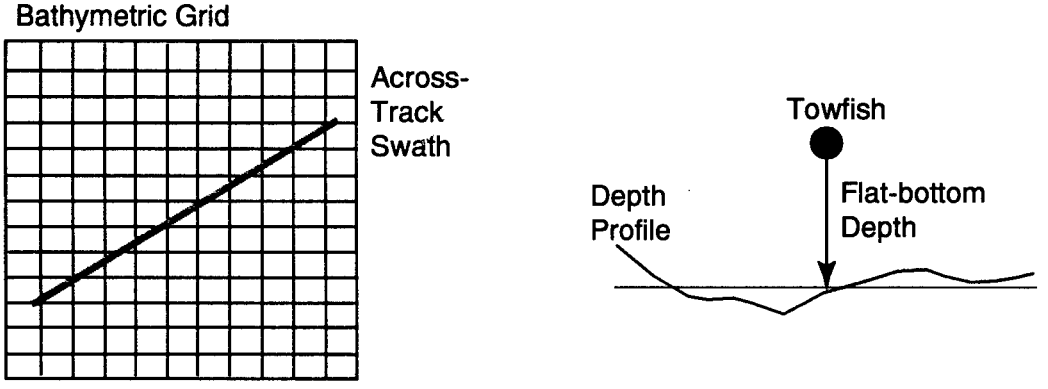

Fig. 22 — On the left is the projection of the across-track coverage of an individual sidescan ping onto a bathymetric grid. An across-track depth profile (right) is then computed by sampling the bathymetric grid values.

The resampling process next obtains the true depth d at some position x_1 (Fig. 23). The slant range R to this position is then computed: $R = \sqrt{x_1^2 + d^2}$. Using this slant range value, the across-track distance x_2 of the original flat-bottom data set is computed as

$$x_2 = \sqrt{R^2 - z^2}, \tag{27}$$

where z is the flat-bottom depth. The pixel value of the original datum at across-range range x_2 is then assigned to the pixel value of the repixelled datum at across-track position x_1. This procedure continues for the entire data set.

An alternative means of repixelling would be to reverse the methodology of the previous section (Fig. 24). In this case, one would select the flat-bottom pixel value at x and would then try to determine the appropriate new position based upon the true seafloor depths. The problem with this approach is that in areas of steep topography, especially close to the nadir, there sometimes exists a non-unique functional mapping. This is shown in Fig. 24 where the original flat-bottom position x maps to two possible locations x_1 and x_2.

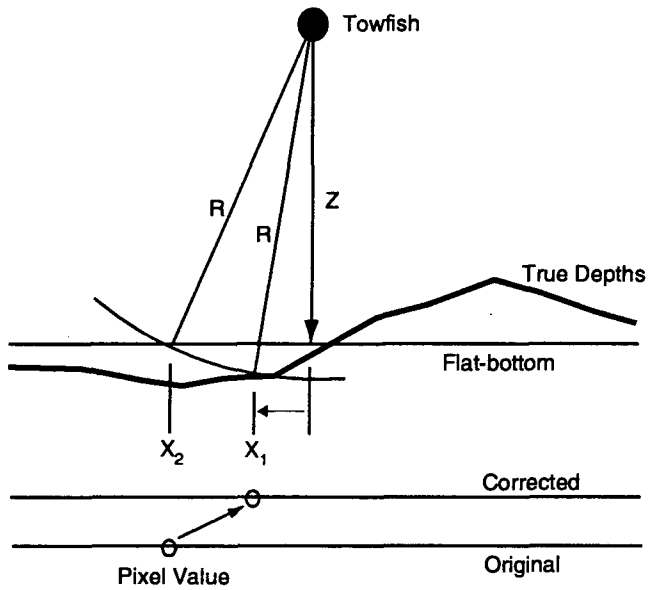

Fig. 23 — Resampling of the original data (flat-bottom) to generate the corrected repixelled image (true depths). The top diagram shows the computation of the slant range *R* for the true bathymetric profile, and the projection of *R* onto the flat-bottom profile. The bottom half of this diagram illustrates the resampling process.

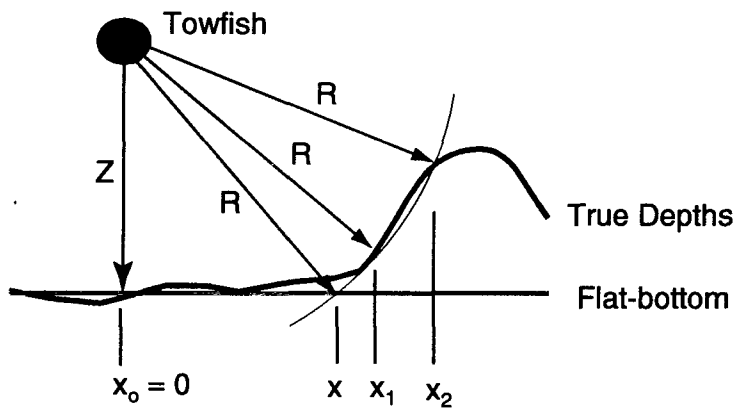

Fig. 24 — Non-unique functional mapping of slant ranges onto real bathymetry. The original flat-bottom point *x* has slant range equal to *R*. Due to the large topographic variations, points 1 and 2 have the same slant range.

6.2.3 Multibeam System Pixel Generation

Acoustic backscatter data from multibeam systems are generated by applying specialized beamforming processing. The beams are first generated using the standard application of the fast Fourier transform (FFT). For SASS, this is accomplished by the spatial FFT of the in-phase and quadrature components of the signal, and the subsequent computing of the amplitude beamformed time series.

The difficult task is to then determine the time of the peak amplitude signal for each beam. This is accomplished by setting some predetermined threshold value and by testing the signal to see if this threshold is exceeded. The angle of arrival is the beam angle θ, which when combined with the slant range time gives the across-track pixel position x,

$$x = \sin(\theta)\, t_r\, c\,, \tag{28}$$

where t_r is the travel time corresponding to the peak amplitude signal, and c is the sound speed of water. The pixel value is simply the peak amplitude of the beam formed time series.

Analysis has indicated that errors in this time of arrival increase as a function of across-track range as the envelope of the return signal becomes more spread out in time [92]. Furthermore, the beam angle represents the theoretical take-off and received angle and does not take into account possible refraction of the propagation path. This latter effect is sometimes significant as hull-mounted multibeam systems operate in the midst of the surface thermocline where large vertical variations in sound speed are present, resulting in increased refraction of the propagating signal.

6.3 Differential Phase Measurement

The deployment of a dual array per side configuration has enabled the collection of bathymetric data by a sidescan system; these instruments are called swath bathymetry or bathymetric sidescan systems. This development was initiated when early sidescan users observed the appearance of interference fringes created by return signal reflecting off the sea surface. It was eventually realized that a second receiver array could be used to estimate the angle of arrival of the signal.

In an interferometric bathymetry system, two or more longitudinal arrays are used to record the return signal from the seafloor. Assuming the signal is coherent at both arrays, the time shift, or equivalently the phase lag between the two waves, is then computed; this difference is often called the electrical phase difference. The conversion of the electrical phase difference $\Delta\phi$ to the geometric or acoustic angle θ is simply [93],

$$\Delta\phi = \frac{2\pi d}{\lambda} \sin(\theta - \theta_m), \tag{29}$$

where λ is the wavelength of the signal, d is the distance between the two arrays, and θ_m is the mount angle of the array with respect to the vertical direction (Fig. 25). In the ideal configuration, d is set at $\lambda / 2$. In this case, the electrical phase angle difference varies between $-\pi$ to π radians (–180° to 180°) with each value corresponding to a unique acoustic angle.

In reality, there are several problems inherent with interferometric systems. Due to engineering restrictions, the arrays are sometimes spaced several wavelengths apart. This configuration is commonly found on high frequency systems where the wavelengths are very small. Under these conditions, the measured phase difference varies through several cycles of $-\pi$ to π, leading to a potential phase ambiguity problem [94, 95]. The number of $-\pi$ to π cycles that exist is equal to the separation distance divided by $\lambda / 2$. To alleviate this ambiguity problem, which can be troublesome in the presence of substantial noise, some systems use a third receiving array that is offset at a different spacing than the other two.

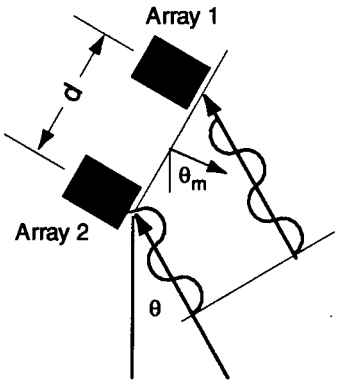

Fig. 25 — Differential phase measurements using two parallel arrays

Another problem that plagues some interferometric systems is that the computed acoustic angle does not necessarily represent the true geometric angle of arrival (Fig. 26). There are several reasons for this discrepancy. Arriving signals are sometimes diffracted by the sharp edges of the various structural elements within the towfish including the array mounts themselves. Furthermore, there can be variations in the signal magnitude received by the two arrays caused by acoustic multipath effects, and by problems in the beam pattern and sidelobes. Finally, there can also be reception of signals from the other side of the towfish. The outcome of all of this is that the signal arriving at the two arrays may be different.

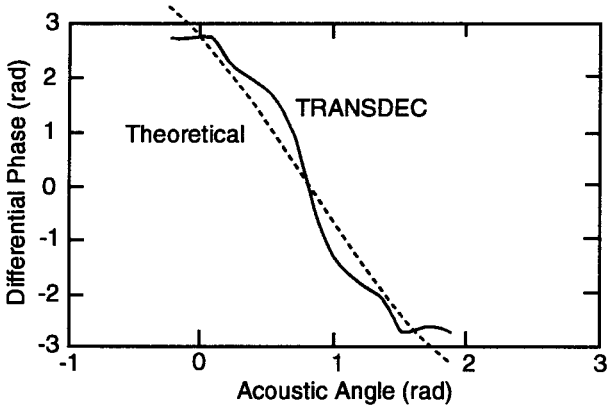

Fig. 26 — Differential phase vs acoustic angle for the SeaMARC II system. The solid line is the result of a calibration measurement at the TRANSDEC facility. The dotted line is based on Eq. (29). Figure from Ref. 96.

The SeaMARC II phase calculations were based on a rather ad hoc time-phase histogram methodology that was subject to potentially large errors. For instance, the time accuracy was based on the size of the histogram bin, which was generally set at 32 ms; being off by a single bin would lead to a slant-range error of 45 m. An improved methodology for obtaining more reliable, noise-resistant phase measurement has subsequently been incorporated in the SEAMAP and HAWAII MR1 bathymetric sidescan systems [96]. The basic technique involves the initial base-banded quadrature

sampling of the signal received by the dual arrays, hereby denoted by subscripts 1 and 2. One representation of the phase difference $\Delta\phi$ between the signal recorded by arrays 1 and 2 is

$$\Delta\phi(t) = \tan^{-1}\left[Q_1(t)/I_1(t)\right] - \tan^{-1}\left[Q_2(t)/I_2(t)\right]. \tag{30}$$

Unfortunately, this formulation involves the non-linear arctangent function and is also susceptible to noise contamination by virtue of the division of the in-phase term I. When I is small, the introduction of noise can easily dominate the phase calculation. To overcome these limitations, deMoustier and coworkers [97] have derived an improved formula for computing the differential phase:

$$\Delta\phi(t) = \tan^{-1}\left\{\frac{\sum_{n=1}^{N} W^2(n)\,\mathrm{Im}\left[s_1(n)s_2^*(n)\right]}{\sum_{n=1}^{N} W^2(n)\,\mathrm{Re}\left[s_1(n)s_2^*(n)\right]}\right\}, \tag{31}$$

where $s_i(n)$ is the signal received by the ith array, * denotes the complex conjugate, W is a window function, n is the sample number of the digitized signal, and N is the number of samples.

6.4 Bathymetric Sidescan Angle / Depth Conversion

As previously noted, the acoustic angle determined by the measured electrical phase difference does not necessarily correspond to the true geometrical angle of arrival. Furthermore, refraction of the signal has also been neglected. To simultaneously overcome both of these problems, systems such as SeaMARC II and SEAMAP have used empirical lookup tables to convert the acoustic angle to the geometric angle.

The computation of the lookup table, also called the angle-angle table, is performed in a fashion similar to that used to compute the empirical angle varying gain correction (Section 6.6.1). This involves first identifying a section of the seafloor that is judged to be flat in the across-track direction. The task then becomes one of computing correction factors that transforms the phase data (acoustic angles) to a constant depth value.

The computation proceeds as follows. Any particular ping has a series of computed acoustic angles θ_a, which are themselves associated with a travel-time value t_a. Given the depth of the seafloor as determined by first bottom-detect, new angles are then computed such that

$$Z = \left(t_a/2c\right)\cos(\,\theta\,)$$

and

$$\theta_n = \cos^{-1}\left(2\,c\,Z/t_a\right). \tag{32}$$

where Z is the first bottom-detect depth, c is the sound speed, and θ_n is the new corrected angle. A mapping is then made between $t_a \Leftrightarrow \theta_a$ and $\theta_a \Leftrightarrow \theta_n$. A series of pings are used in the calculations with an ensemble average computed to reduce the effect of noisy data. Additional filtering can also

be performed. The final angle-angle table is the mapping $\theta_a \Leftrightarrow \theta_n$ (Fig. 27). This type of calculation implicitly factors refraction effects into the correction tables.

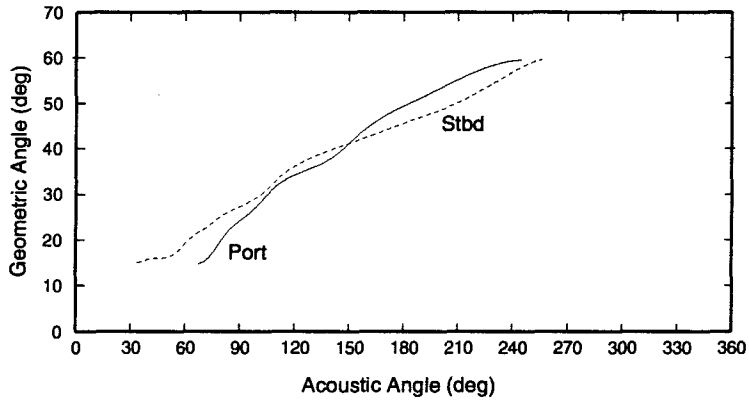

Fig. 27 — A typical empirical angle-angle table used to convert the received acoustic angle to a geometric angle

6.5 Time-Varying Gain (TVG)

The propagation of acoustic waves results in the decrease in intensity in a singular direction due to combination of geometric spreading and attenuation. For the case of geometric spreading, the outgoing and return signals undergo a deterministic spherical spreading loss. This loss is an inverse square range relationship or equivalently inverse square time if the sound speed is essentially a constant. The additional effect of attenuation (absorption) is a little bit more complicated as it is dependent on the environmental conditions of the propagation medium. However, one can still adequately assume some average absorption coefficient dependent on the frequency of the transmitted signal and compute a TVG function that compensates for the transmission loss.

Most acoustic imaging systems incorporate a TVG correction in the data acquisition hardware or software at the stage before the analog-to-digital conversion. From a practical basis, this is performed because A/D converters are limited by their fixed dynamic range; it is necessary to amplify the signal to avoid discretization or clipping A/D problems. One problem that arises from the application of a TVG function is that ambient noise is increasingly amplified as time progresses. TVG amplified noise is most prevalent at the outer edges of the swaths.

6.6 Angle-Varying Gain (AVG)

The across-track intensity of acoustic backscatter data depends on several factors that are functions of the ensonification angle. First, the transmitted acoustic signal is preferentially steered to have its maximum intensity in some predefined vertical elevation angle. This element is designed into sidescan systems to ensure the selective ensonification of a section of seafloor away from the nadir. Furthermore, the beam pattern is usually designed to minimize the energy that is transmitted in the vertical direction; this reduces the introduction of water multiple arrivals. These artifacts can be rather significant due to the greater amplitude of specular reflection with respect to scattering. Hence, as the transmit beam pattern is unevenly distributed, the intensity of the returned signal is also unevenly distributed.

In theory, one could measure the transmit beam pattern *a priori*, and then apply an appropriate correction factor. However, this is not always a feasible option. For instance, low-frequency acoustic imaging systems are usually calibrated by measuring only the near-field transmitted beam pattern. Unfortunately, it is the far-field acoustic beam pattern that is needed and the measurement of this would require the use of a relatively large calibration facility. There is also the need to understand or measure what effect changes in hydrostatic pressure and temperature have on the transducers and hence their effect on the beam pattern. Furthermore, the receive beam pattern of the imaging system also needs to be known and corrected for in a manner similar to that for the transmit signal.

Another effect that produces angular variations in the received signal is the angular dependence of the backscatter process itself. For instance, an adequate first-order representation of the backscattering from the seafloor is the Lambertian scattering distribution given by

$$I = I_0 \cos^2(\theta) , \tag{33}$$

where I_0 is the scattering strength and θ is the ensonification angle with respect to the vertical direction. From this relationship, one can infer that the backscattering steadily decreases from the nadir position to the outer edge of the swath. It also needs to be pointed out that refraction effectively causes the value of θ at the towfish to be different than that at the seafloor. However, if the sound speed at the source and seafloor are known, then one could easily compute the θ at the seafloor by using Snell's law; no ray tracing is required.

6.6.1 AVG Correction

For the vast majority of acoustic swath imaging systems, an empirical AVG correction is computed and applied during the post-processing stage. While this correction is rather straightforward, it does require making one very important assumption that then conditions the interpretation of the resultant imagery data. Given a section of seafloor that is assumed to be relatively flat and homogenous in its backscattering strength, one first computes the ensemble average of the received intensities as a function of ensonification angle. One then explicitly defines what this angular distribution should actually be. For instance, a standard assumption is to prescribe a uniform intensity as a function of angle. The angle varying gain correction *avg* is then given by

$$avg(\theta) = \frac{\sum_{j=1}^{n(\theta)} p_j(\theta)}{n(\theta)\,\overline{p}}$$

and

$$\overline{p} = \frac{\sum_{j=1}^{N} p_j}{N} , \tag{34}$$

where $p_j(\theta)$ is the i^{th} intensity value for a given angle θ, $n(\theta)$ is the number of intensity values for angle θ, and N is the total number of values. The use of this function produces imagery data characterized by uniform across-track values. This transformation essentially converts the data to have a common ensonification angle (Figs. 28 and 29).

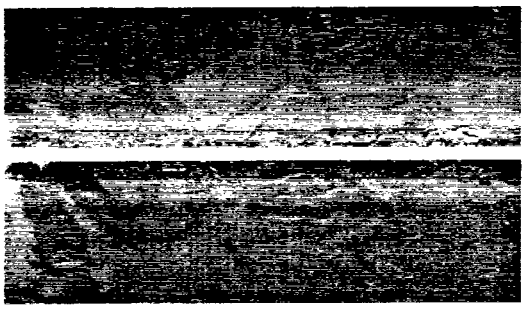

Fig. 28 — Sidescan track data prior to applying an AVG correction. The track proceeds from top to bottom with the lighter gray shades representing weaker returns.

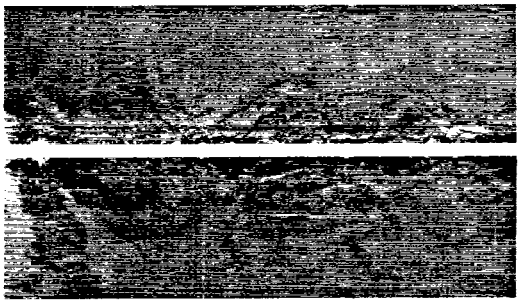

Fig. 29 — Sidescan track data after applying an empirical AVG correction

Other assumptions can be made that better retain the true acoustic backscattering information of the data. For instance, assume once again that the seafloor is flat and homogeneous in its backscattering strength. An assumption of the angular dependent backscattering properties of the seafloor, such as Lambertian scattering, can then be made. The AVG function that would match the data to such a relationship can then be computed. It is obviously important to know what AVG correction function was applied if one wants to extract meaningful acoustic backscattering information from the data.

6.7 System Parameter Corrections

The user can usually control several parameters to optimize the operational performance of sidescan and multibeam systems. These parameter adjustments are required to compensate for changes in the survey environment such as water-depth and geologic tectonic regime. Hence, parameters such as ping-rate, transmit power, receive gain, pulse width, and the output pixel size are usually set by the on-board personnel during a survey. In theory, the proper design, implementation of the system engineering, and recording of these parameters means that these changes are deterministic and can therefore be compensated for in the post-processing stage of analysis. In cases where the parameters are improperly recorded or are inaccurate, empirically derived corrections are required.

6.8 Destriping

A common artifact in acoustic imagery data is the presence of pings characterized by lower than average intensity values. These low valued ping dropouts are caused by a combination of factors such as low-intensity transmitted pulses or the misorientation of the imaging platform during the transmission and reception of the signal. One should note that higher average intensity pings are less common.

One reason for the presence of low-intensity ping values is simply the inefficient or ineffective transmission of the outgoing acoustic pulse. This can be caused by inconsistent firing of the transducers, or inconsistent discharge of the storage capacitors for low-frequency systems. In this regard, higher intensity transmitted pulses are not expected as most systems are designed to generate

pulses that are close to the cavitation limit of the transducer design. For the case of multibeam imagery, adapted gain control of the transmit pulse is sometimes incorporated into the system design; SASS Phase IV is an example of such a system. This adapted gain needs to be measured, recorded, and subsequently corrected for in the post-processing stage. Needless to say, if the gain is measured incorrectly, the correction is inaccurate.

A more common reason for the generation of ping dropouts is an inordinately large movement of the imaging system during the transmit and/or receive period of operation. This effect is better understood if one considers the purposeful design of the arrays to transmit and receive signals in a narrow athwartship horizontal beam direction. If this directional beam is misaligned (in pitch or yaw) during either transmit or reception, then low intensity signals are commonly recorded (Fig. 30). This misalignment typically occurs while surveying in rough sea states where severe heaving of the towing platform takes place. This motion transmits erratic forces on the towing cable that generate unacceptable motion of the imaging system. The rolling motion of the platform does not create ping dropouts.

There have been several methodologies proposed for destriping acoustic imagery data that are characterized by ping dropouts. To the first order, one could simply compute the average intensity value of all the across-track pixels per ping, and then filter this ping average function to remove the outliers. The correction would then be the difference between the filtered averaged and the original values. A high-order correction has also been proposed whereby orthogonal functions (e.g., Chebyshev polynomials) that describe the across-track pixel intensities are computed [98]. Subsequently, the coefficients of these orthogonal functions are then filtered, with the correction once again being the difference between the filtered and the original values.

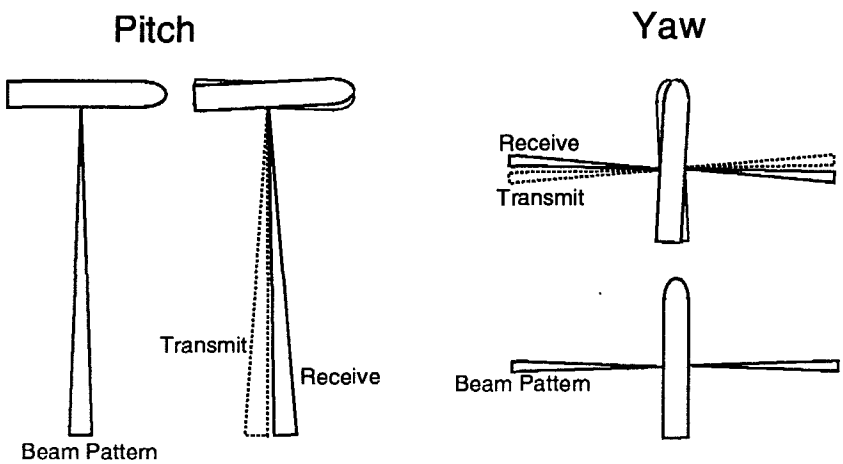

Fig. 30 — Misorientation of the transmit and receive beams caused by the pitch and yaw motion of the imaging platform. Low intensity returns are recorded when the beams do not overlap.

6.9 Contrast Mapping and Enhancement

To display acoustic imagery, the data intensity value needs to be converted to some color or gray

scale value. Selection of the appropriate color lookup table (LUT) is somewhat arbitrary and is usually chosen to optimize the interpretation of the data by the naked eye. This transformation can also be selected to show the acoustic information content, enhance the identification of targets, or optimize geological interpretation.

Histogram equalization is a very common technique used to enhance the visual analysis of acoustic data to interpret geological features. In this standard image processing technique, data values are transformed so that the probability function of a pixel having a particular intensity value I is a constant for all intensity values. Hence,

$$\text{Prob}(I) = \frac{1}{I_{max} - I_{min}}, \tag{35}$$

where I_{max} and I_{min} are the maximum and minimum intensity levels of the data. Alternatively, other histogram functions such as an exponential distribution or a logarithmic distribution shown below can be used.

$$\text{Prob}(I) = \alpha \exp[-\alpha(I - I_{min})] \qquad \text{(exponential)}$$

$$\text{Prob}(I) = \frac{1}{I\left[\ln(I_{max}) - \ln(I_{min})\right]} \qquad \text{(logarithmic)} \tag{36}$$

6.10 Spatial Filtering

Acoustic backscattering imagery, like that of SAR imagery, is characterized by the presence of speckle. This speckle is generated by the random phase nature of scattering from a field of random scatterers, and can also be generated from environmental noise factors. If the characteristics of the speckle are indicative of the statistical components of the scattering field, spatial filtering essentially eliminates what could be useful information from the data merely to produce an aesthetically pleasing image. There are many spatial filtering techniques, most of which have been adopted from optical image processing [99, 100]. Of these, probably the fastest and easiest method for reducing speckle is to apply a 1-D or 2-D median filter to the imagery data.

6.11 Acoustic Shadows

Under certain imaging conditions, topographic relief may block acoustic propagation, thereby causing acoustic shadows (Fig. 31). These shadows are especially common when the imaging system is deployed at a shallow altitude over the seafloor. Since shadows are distinct features whose attributes are a function of the imaging geometry, their characteristics can be used to extract information about the height of the blocking object.

If the imagery data is positioned using the flat-bottom assumption with assumed depth z, then the shadow depicted in Fig. 31 extends from x_1 to x_2. The height of the feature is then determined by first computing the slant range of the position x_1:

$$r_1 = \sqrt{x_1^2 + z^2}\ . \tag{37}$$

Assuming that position x_2 is at a depth equal to z, the incident angle is given by

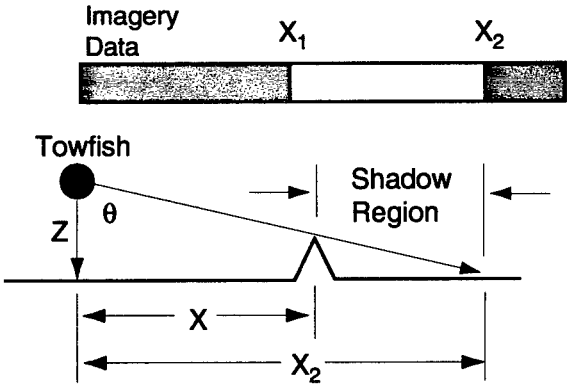

Fig. 31 — The illustration at the top represents the begin and end points of an acoustic shadow. The bottom drawing shows the geometry that produces the shadow. Note that position x_1 in the imagery data is offset from the true position x due to the flat-bottom assumption.

$$\theta = \tan^{-1}(x_2 / z) . \tag{38}$$

The height h and position x of the object are simply

$$h = z - R \cos\theta \tag{39a}$$

and

$$x = r_1 \sin\theta . \tag{39b}$$

6.12 Geocoding

Acoustic backscatter imagery data are collected by recording the across-track signals generated by discrete transmitted pulses. These time-encoded ping data are subsequently merged with navigation information (latitude, longitude, and heading), which describes the spatial orientation of the data. After the selection of the appropriate coordinate system, geographic boundary limits, and grid size, geocoding begins by placing the track acoustic data into the individual grid cells after applying the proper coordinate transformation function. This conversion of scanline data to a geographic spatial distribution is termed geocoding and is discussed in detail in Section 7.

7. ACOUSTIC IMAGERY MOSAICS

Advances in computer technology related to data storage and processing capabilities have enabled the practical generation of composite digital mosaics of acoustic imagery data. These mosaics represent the coordinate transformation of the time-coded track data to a geocoded series of grid cells. When geocoded, acoustic imagery data can be effectively combined with ancillary information, such as bathymetry, to optimize the end-user's capability to interpret the data.

The gridding of backscatter data differs significantly from the gridding of bathymetric data. Unlike bathymetric data, little effort is made to fill in data gaps except in the areas between successive

pings; these data gaps are simply left blank (null). Secondly, due to the angular dependence of backscatter, caution must be used such that data from multiple look directions are not combined into a single grid cell. For instance, a sloping section of the seafloor can be imaged in the up or down slope directions depending on the location of the sensor. Averaging returns from up and down slope backscatter data tend to cancel out and results in a fairly muted or distorted acoustic image.

7.1 Tiles

Acoustic backscatter intensity is dependent on the frequency of the transmitted pulse and the ensonification direction. Therefore, it is usually difficult to combine data from different mapping systems and different surveys into a single composite mosaic. Hence, backscatter mosaics are best generated using only data collected from one system where the coverage consists mainly of uniformly spaced parallel tracks.

There are times when there exist overlapping acoustic imagery data from multiple mapping systems within a particular geographic area. To accommodate this overlap, the data should be partitioned into individual data sets (tiles) that are aligned in some coordinate system. These tiles can be of different size and shape to allow for differences in the inherent spatial resolution of the frequency-specific data. An example of a series of tiles in a particular geographic region is shown in Fig. 32.

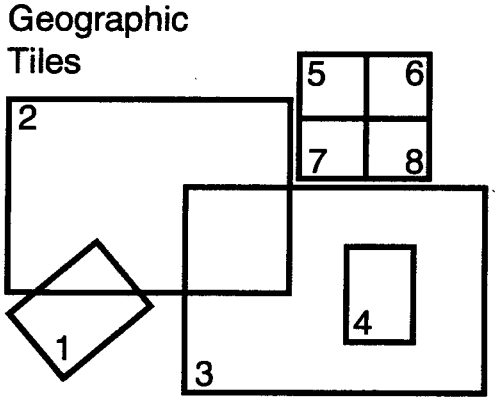

Fig. 32 — Multiple tiles within a particular geographic area. An individual tile corresponds to data collected with one system and one track orientation.

7.2 Cells

A normal tile consists of individual cell units that are aligned in an orthogonal orientation that mimics the boundary of the tile; in other words, rows and columns (Fig. 33). The number of rows and columns are user specified and can vary between different tiles. The maximum number of rows and columns that a tile contains should be selected to optimize data storage, retrieval, and organization. For instance, in Fig. 32, tiles 5, 6, 7, and 8 represent mosaics from a single system, single cruise. In this example, the use of a single tile was for some reason deemed to be non-optimal, so multiple tiles were used instead.

The cells themselves can consist of multiple data layers. The primary layer is naturally the backscatter imagery data values. In certain cases, there are no data associated with particular cell. In this absence, the cell value is assigned a preassigned null value. An optional layer in a cell could consist of the azimuthal angle of ensonification or the ensonification angle in the vertical direction. These values are useful to the end-user as they provide information that is vital for the proper interpretation of the imagery data.

Finally, a data layer that gives the position errors can also be embedded in a cell. These error covariances can be encoded on a cell by cell basis, or conversely, can be a data flag indicating some error value province. All cells with the same province value are parameterized by the same position error. If provincing is used, then some position error lookup table needs to be available. This error table could be tile-specific and encoded in the data file header, or could conversely be universal for all tiles. In the latter case, only one position error LUT is needed, and this LUT could be stored separately from the tile in an accessible place. Additional flexibility can be obtained by using a series of universal position error LUTs, or by specifying a position error scaling factor term.

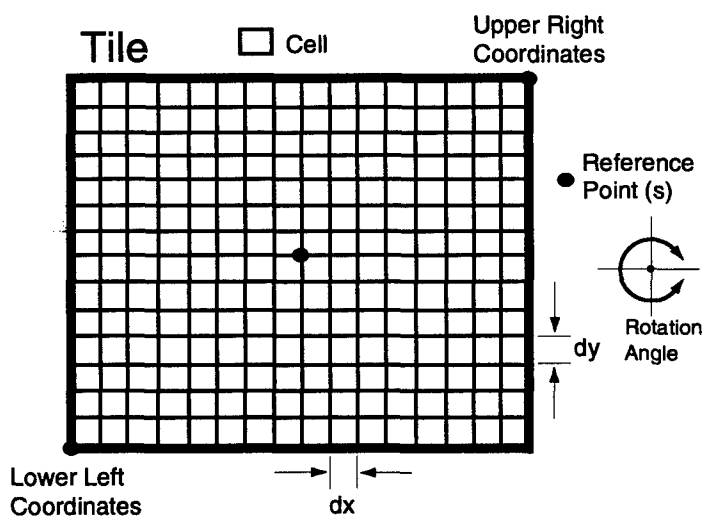

Fig. 33 — Some components and parameters of a tile and its associated cells

7.3 Coordinate Space

Geocoding requires the selection of either a geographic or map projection coordinate system and the requisite minimum set of parameters that describe such a system. Commonly used map projections are Mercator, Universal Transverse Mercator (UTM), and polar stereographic. Each of these transformations requires a different set of parameters to characterize the mapping system. In general, all geocoding transformations require the following information:

1. geographic or map coordinate system reference points (e.g., latitude and longitude)
2. grid spacing in the tile's horizontal and vertical directions
3. number of rows and columns (Y and X) in the tile

In actuality, the information given by the listed parameters can be determined if alternative pieces of information are encoded instead. For instance, the geographic or map coordinate locations of the four corners of the tile along with the number of rows and columns are sufficient to deduce the grid spacings.

For some map coordinate transformations, additional information is required. These additional parameters include

1. rotation angle about some reference point,
2. projection points (e.g., polar stereographic), and
3. reference ellipsoid vs spherical Earth.

7.4 Gridding Algorithm

Gridding of acoustic imagery data is much different than that performed on bathymetric data. Invariably it involves either smoothing, decimating, or both processes, with very little extrapolation of data values outside the spatial range of the original track swath coverage. Additionally, care must be taken so that data characterized by different ensonification directions are not combined. Furthermore, one needs to be wary of combining data collected by imaging systems with different transmit frequencies and spatial resolutions.

One simple gridding technique is a LILO (last in, last out) algorithm that is analogous to FIFO (first in, first out), commonly found in the computer industry. In this methodology, a map projection coordinate system is initially specified along with the tile's boundary and grid spacing. An individual acoustic imagery datum is then geocoded and assigned to the appropriate cell that corresponds to the geocoded coordinates (Fig. 34). This procedure continues for all the data. If duplicate data are assigned to the same cell, then only the last value is used; all data previously residing in that particular cell are discarded. Hence, the order in which the data are geocoded plays an important role in the final makeup of the mosaic. Note that choosing the inverse rule of the first datum to be the final cell value is simply equivalent to reversing the order in which the data are gridded using the LILO rule.

An alternative gridding method would be to perform a similar type of geocoding except that the final cell value would be the mean or median value of all the data associated with that cell. The use of the median value might offer some benefits towards the suppression of speckle. A modification to the aforementioned gridding methods can also be incorporated such that a datum can influence the value of adjoining cells. Up to this point, it has been assumed that a particular datum is a spatial point function. To enhance data smoothing, a broader spatial function can be incorporated into the gridding algorithm. The simple averaging function now becomes a weighted average, with the weights being the value of this function.

For cases where the cell size is smaller than the spacing between data points (e.g., as in Fig. 35), the spatial averaging method may prove to be non-optimal, while the LILO would generate a large number of local null cells. Therefore, a different approach to computing the cell values is desirable. A simple method would be to first determine which cells reside within the area of the track coverage. The nearest data points for each cell are then identified. The cell value could be the average of the bounding data points, a weight average based on distance to the cell, or simply the value of the datum closest to the cell. The procedure would continue until all cells values within the track coverage were computed.

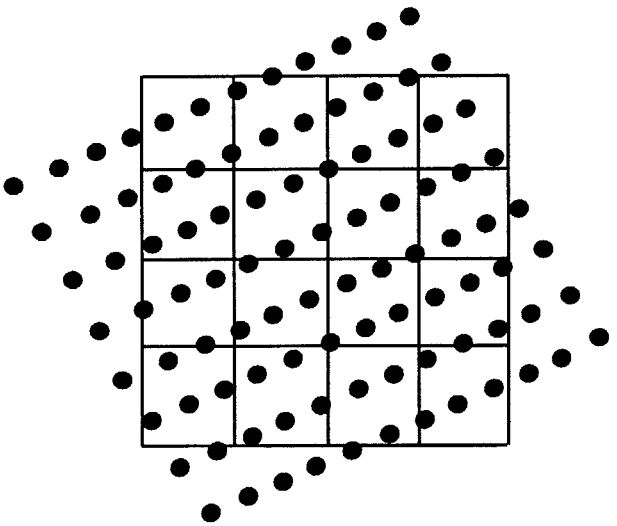

Fig. 34 — Imagery data points (dots) overlaying a series of cells (boxes). The spacing of the original data is smaller than the cell size. In this example, geocoding reduces to a problem in decimation (LILO) or averaging.

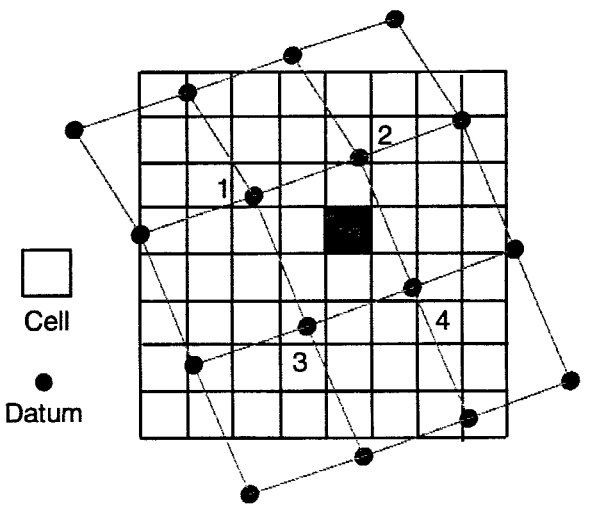

Fig. 35 — Geometry for interpolating a cell value. The featured cell (shaded cell) and the four closest data points are displayed. The value of the cell could be computed by taking a weighted average of data points 1, 2, 3, and 4.

Invariably, difficulties arise in generating continuous coverage acoustic imagery grids when navigation turns are encountered. Like bathymetric data, there is duplicate coverage on the inner section of the turn, while the outer areas have sparse coverage (Fig. 36). However, unlike bathymetry, acoustic backscatter imagery data values are ensonification direction dependent. Therefore, a problem arises into how one should combine the duplicate data on the inner section of the turn because of the different ensonification directions. Furthermore, the sparse data coverage on the outer

areas of the turn usually leads to small data gaps. The geocoding of data at navigation turns likely requires the use of the LILO method in the overlap region, and the interpolation method on the outer edges. Finally, it is well known that platform stability, especially that of a tow system, is greatly degraded during turns, and substandard acoustic imagery data are often collected.

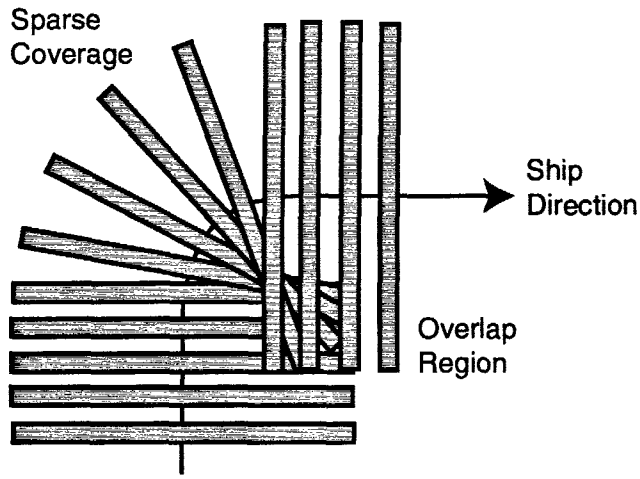

Fig. 36 — Placement of swath data during a navigation turn. The inner area of the turn has duplicate data characterized by different ensonification angles. The outer edge of the turn has relatively sparse data coverage.

7.5 Cell / Grid Size

The optimal grid size of an acoustic imagery mosaic is one that maintains the information content of the data while also minimizing the storage requirements. Therefore, a potential choice for selecting the cell size is to choose a value based on along and across-track data spacings while also factoring in the effect of the pulse width and beam patterns.

7.6 Errors in Geocoding

Position errors in geocoding are primarily a function of errors in the navigation and platform orientation information. Additionally, errors are also introduced by propagation refraction effects and by deficiencies in the flat-bottom assumption. Section 9 discusses these factors in greater detail.

7.7 Data Compression

As opposed to spatial point data, mosaics typically contain cells in which there are no data (i.e., null values). Hence, data compression algorithms are usually beneficial in reducing the data storage requirements while maintaining data integrity. While a host of compression algorithms are available, experience has indicated that primary reduction in the stored size of the data comes from the compressing of the null data cells. For backscatter imagery data values, however, the ubiquitous presence of speckle makes the actual data too "jittery" to allow much size compression.

8. IMAGERY ARTIFACTS

Several common types of artifacts can appear in backscatter acoustic imagery data. In general, these artifacts are easy to identify and their origins are well known. Unfortunately, it is not always trivial to eliminate these artifacts.

8.1 Crosstalk

It is not possible to determine whether signals received by a horizontal line array originated from either the port or the starboard side. This left-right ambiguity is the primary reason why sidescan systems are designed to have separate directional port/starboard side receiving arrays and why these transducer arrays transmit at different frequencies. In a perfect system, the directionality of the receive beam pattern is null towards the opposite side of towfish, thus eliminating port/starboard crosstalk. In practice, however, there are usually minor sidelobes in the beam pattern. Hence, signals coming from the port side are received by the starboard arrays, and vice versa. While these sidelobes are smaller in amplitude than the main direction lobe, strong signals from the opposite side of the towfish could be received with sufficient intensity to appear on the image data (Fig. 37). Thus, crosstalk is most noticeable when there are strong backscatterers (e.g., large sloping features facing the towfish) on one side of the platform and benign weak scatters on the other side.

The problem with crosstalk is lessened by using port and starboard transmitters with non-overlapping frequency bandwidths. For instance, such systems as SeaMARC II, SEAMAP, and MR1 use an 11 kHz port frequency and a 12 kHz starboard frequency. Unfortunately, as in the case of SeaMARC II, the normal operating pulse width was 1 ms, which results in an effective bandwidth of 1 kHz. Hence, the port and starboard transmit frequencies overlap, thus making crosstalk possible. If the transmit pulse length were increased, however, the equivalent decrease in bandwidth would drastically reduce the crosstalk problem.

Fig. 37 — Crosstalk artifacts in the sidescan data appear as mirrored overprinting images of a feature from one side to the other side

8.2 Interference

It is now a common practice to operate a sidescan system simultaneously with other acoustic seafloor mapping instrumentation such as a multibeam or 3.5 kHz echo-sounding system [101]. This requires configuring the timing sequence of the multiple sources to preclude signals from one system from interfering with the reception of another system's signals. Consideration is also given to the frequencies of the various transmitted pulses and to the effective bandwidth of the receivers. In theory, when the frequencies do not overlap, the different equipment can operate simultaneously.

In practice, interference from another acoustic source is sometimes recorded by the sidescan system (or multibeam system). This usually occurs when the controlled multiple firing sequence is changed (or not changed) to adjust for changing water depth. At times, unfortunately, this sequence is not optimal, as shown in Fig. 38. In this example, 3.5 kHz echosounder signals are overprinted onto SeaMARC II sidescan data. The effect of the TVG correction is readily apparent in the increase in the intensity of the 3.5 kHz signal towards the outer edges of the swath.

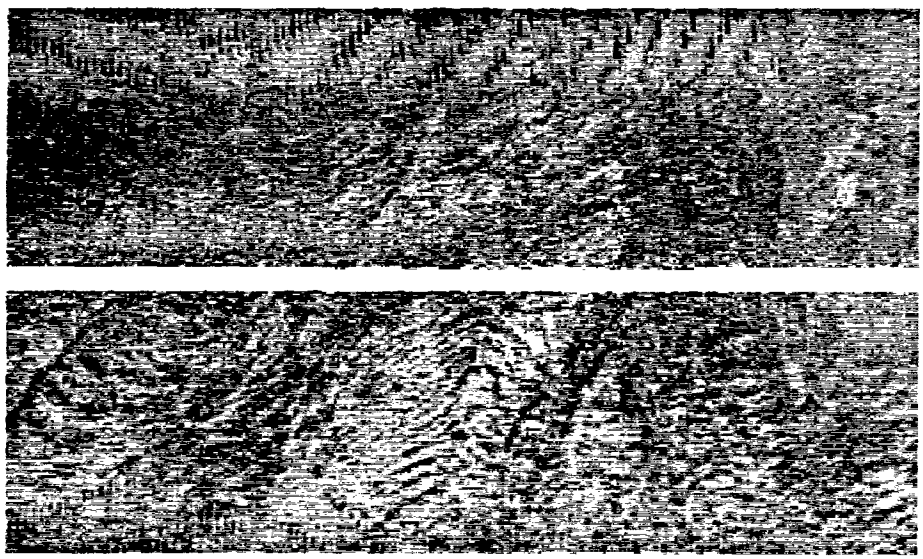

Fig. 38 — Example of 3.5 kHz interference overprinting sidescan data. This interference appears as vertical tick marks in the imagery.

8.3 Water Bounce Multiples

Sidescan systems are designed to minimize the transmitted energy focused directly under the towfish; this decreases the amount of strong specular reflections from the seafloor. These reverberations, if not suppressed, can produce multiple water bounce arrivals that are overprinted onto the backscatter data [102]. One should note that in a manner similar to that of the problem of crosstalk, the transmitted and receive beam patterns usually have sidelobes in the vertical direction. Figure 39 shows several possible multiples.

The first water bounce multiple is the path in which the pulse reflects off the seafloor and the sea surface. This signal is received by the arrays at a time shortly after the first arrival from the seafloor.

This time lag is simply $2D/c$, where D is the depth of the towfish and c is the average sound speed. For shallow towed systems, this artifact would appear close to the nadir (Fig. 40). Additional water bounce multiple artifacts are created by pulses that reflect off the seafloor more than once.

Another artifact caused by water bounce multiples is an interference pattern commonly observed over a smooth sedimented seafloor in relatively shallow water (Fig. 41). As opposed to the previously described multiples, the propagation path of this artifact is offset with respect to the vertical angle (Fig. 39, lower right). The propagation path consists of oblique angle reflections from the seafloor and sea surface, and finally, backscattering at the outer edges. It is also likely that this artifact is created by the reverse path where backscattering occurs first, then the reflections. Interference fringes are then generated depending on the in-phase coherence of the reflected signals.

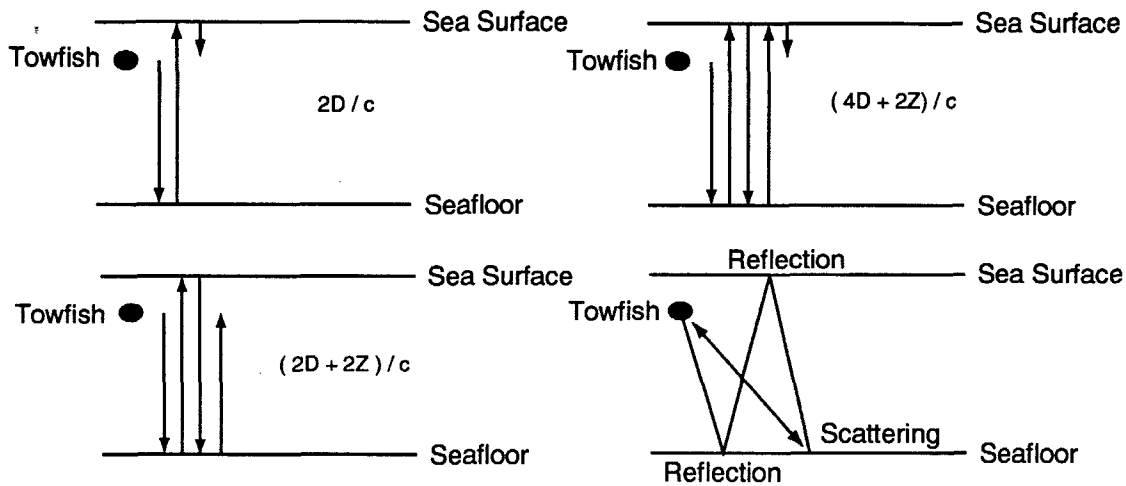

Fig. 39 — The propagation path of water bounce multiples

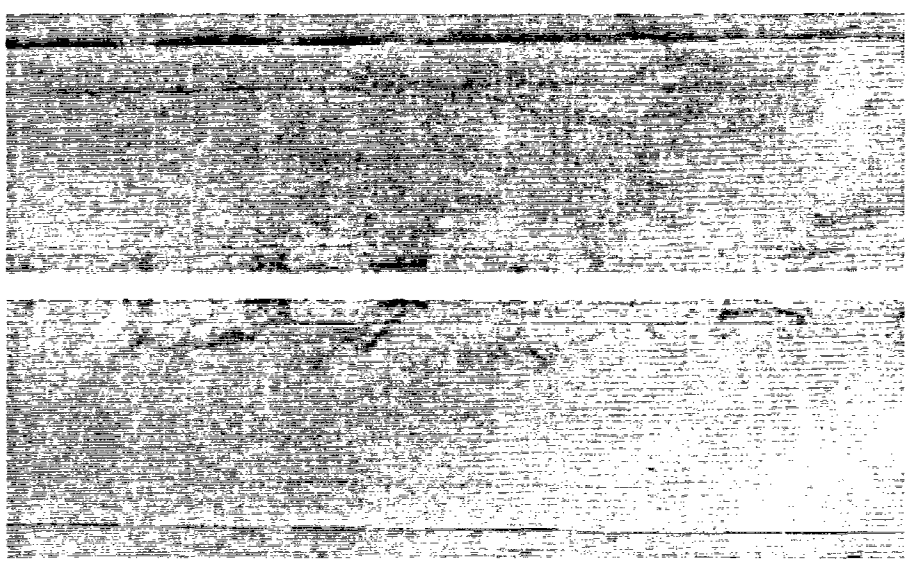

Fig. 40 — Example of reflection multiples in sidescan data. These appear as strong along-track received signals.

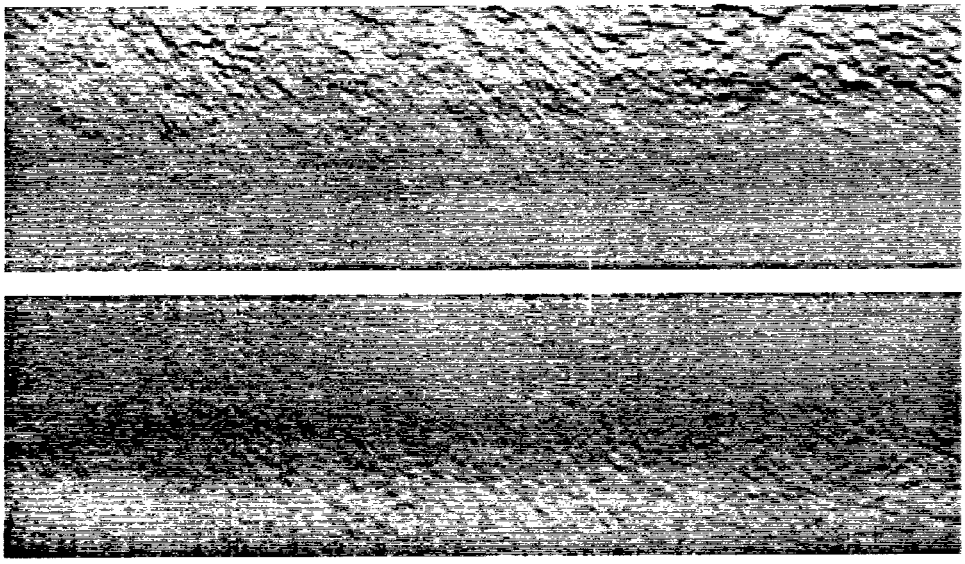

Fig. 41 — Interference pattern artifact on the outer edges of the swath created by multiple reflections off the seafloor and sea surface, and the backscattering at the outer edge of the swath

9. POSITION ERROR

Like all remotely sensed data, acoustic backscattered imagery is subject to position errors caused by inaccurate knowledge of both the imaging platform's position and imaging geometry. Additionally, processing methodology can also introduce errors; e.g., if the flat-bottom or the straight propagation path assumptions are incorrect. These errors can be quantified to some level of precision either theoretically or empirically. This section presents an analysis of the sources of position error for both multibeam and towed sidescan systems.

9.1 Ship Position

To the first order, the navigational accuracy of the ship, whether it be the actual data acquisition platform (e.g., hull-mounted system) or the towing platform for a deployed system, directly affects the position accuracy of acoustic imagery data. Factors that affect ship navigation are the quantity and quality of satellite position updates (e.g., from GPS), shore-based position updates (e.g., from LORAN), and the ship's inertial navigation system.

The most common method of evaluating the accuracy of a ship's navigation is comparing data values (e.g., bathymetry, gravity) at track crossing points. For instance, swath bathymetry data at a track crossing can be spatially shifted so that the data associated with the two tracks match. This computed value is a relative shift that must then be merged with absolute position information, such as GPS fixes, to then generate the best estimate of the ship's navigation [103]. The effectiveness of this methodology is dependent on the magnitude and spatial pattern of the seafloor bathymetric relief. For instance, in a flat featureless area, the bounding error limits of the spatial correlation are relatively large, while in areas of high relief, the bounding errors are relatively small. In one analysis using rather noisy SeaBeam data, average cross-over errors on the order of about 50 m (50% confidence interval) were achieved by the spatial correlations.

9.2 Towfish Relative Position

Many acoustic imagery data collection systems are housed in towfishes that are deployed behind a ship on a cable. Hence, an additional source of position error is inaccuracies or incomplete knowledge of the relative position of the towbody with respect to the towing platform. Some of the factors that contribute to position errors are illustrated in Fig. 9, and include

1. distance (layback) of towfish behind ship,
2. across-track displacement of towfish with respect to the straight-line track of the ship, and
3. misalignment (pitch, roll, and yaw) of the towfish.

The layback of the deployed imaging platform from the towing ship is often an assumed factor. Unless a short baseline acoustic transponder system is deployed, no direct measurable indication of the towfish position is known. Furthermore, while knowledge of the amount of cable deployed from the ship to the towfish may be known, as well as the depth of the towfish, rarely in practice has the geometry of the tow cable been computed. Instead, experience with a particular system and its mode of operation has eventually allowed for the estimation of the layback. Other methods for computing the towfish's relative position are presented in Sections 9.4 and 9.5.

On the other hand, the across-track displacement of the towfish that is caused by the presence of cross-currents is often ignored. In most cases, this is not a significant factor for large, low-frequency systems that are normally towed at fast speeds. However, lighter weight, high-frequency mapping systems, especially when towed at slower speeds, are subject to pronounced lateral displacement in the presence of strong currents.

9.2.1 Propagation of Errors

The errors associated with the towfish's relative position can be easily combined with the absolute position errors of the towing platform by linear propagation of errors. For instance, suppose that the position error of the towing ship at an arbitrary time is given by the bounding errors σ_y, σ_x, and the correlation function ρ. The error distribution of the ship's position $\sigma(x,y)$ is given by

$$\sigma(x,y) = \frac{(x-x_o)^2}{\sigma_x^2} - 2\rho\frac{(x-x_o)(y-y_o)}{\sigma_x\sigma_y} + \frac{(y-y_o)^2}{\sigma_y^2} \tag{40a}$$

and

$$\rho = \frac{\sigma_{xy}}{\sigma_x\sigma_y}, \tag{40b}$$

where x_o and y_o are the longitude and latitude of the ship.

The relative error associated with the towfish's position with respect to the ship has an identical form as Eq. (40); the towfish covariances are hereby denoted by β. The absolute position of the towfish (p) given the absolute position of the towing platform (p_{ship}) and the displacement of the towfish from the ship (Δp_{tf}) is simply

$$p(x,y) = p_{ship}(x,y) + \Delta p_{tf}(x,y) \tag{41}$$

or, since the x and y coordinates can be decoupled,

$$p(x) = p_{ship}(x) + \Delta p_{tf}(x)$$

$$p(y) = p_{ship}(y) + \Delta p_{tf}(y). \tag{42}$$

These linear relationships simply mean that

$$\frac{\partial p(x)}{\partial p_{ship}(x)} = \frac{\partial p(x)}{\partial \Delta p_{tf}(x)} = \frac{\partial p(y)}{\partial p_{ship}(y)} = \frac{\partial p(y)}{\partial \Delta p_{tf}(y)} = 1$$

$$\frac{\partial p(x)}{\partial p_{ship}(y)} = \frac{\partial p(y)}{\partial \Delta p_{tf}(x)} = \frac{\partial p(x)}{\partial p_{ship}(y)} = \frac{\partial p(y)}{\partial \Delta p_{tf}(x)} = 0 \tag{43}$$

The standard linear propagation of errors that gives the final positional covariance matrix **V** is given by (bold letter indicates matrices, superscript T indicates the transposed matrix)

$$\mathbf{V} = \mathbf{A}\,\mathbf{W}\,\mathbf{A}^{\mathrm{T}}, \tag{44}$$

where $A_{ij} = \partial d_i / \partial m_j$, $d_i = \{\, p(x), p(y) \,\}$, and $m_j = \{\, p_{ship}(x), p_{ship}(y), \Delta p_{tf}(x), \Delta p_{tf}(y) \,\}$. The matrix **W** is the combination of the covariance matrices for the ship and towfish positions:

$$\mathbf{W} = \begin{pmatrix} \sigma_x^2 & \sigma_{xy} & 0 & 0 \\ \sigma_{xy} & \sigma_y^2 & 0 & 0 \\ 0 & 0 & \beta_x^2 & \beta_{xy} \\ 0 & 0 & \beta_{xy} & \beta_y^2 \end{pmatrix}, \tag{45}$$

where all σ's are the covariances of the ship, and β's are those of the towfish. The final combined error terms ε are

$$\varepsilon_x = \sqrt{\sigma_x^2 + \beta_x^2} \tag{46}$$

$$\varepsilon_y = \sqrt{\sigma_y^2 + \beta_y^2} \tag{47}$$

$$\varepsilon_{xy} = \sigma_{xy} + \beta_{xy} \tag{48}$$

Equations (46) through (48) give the absolute position error of the towfish. The use of linear propagation of errors can also be used for combining additional independent sources of errors.

9.3 Towfish Platform Stability

The stability of a towed system has a direct impact on both the quality of acoustic imagery data and on the position accuracy of the data [104, 105]. Section 6.8 briefly discusses the effect of pitch and yaw motion on data quality. This is of interest in analyzing position error. While a good first order assumption is that poor quality data (e.g., presence of low intensity stripes) are also

characterized by poor positioning, the inverse of this is not necessarily true. Good quality data can also be poorly positioned.

One possible source of position error is the presence of a systematic skew of the towfish in the along-track direction (yaw). Potential geocoding errors arise if the ship's course instead of the towfish heading is used when gridding the data collected under this condition. The use of an improper heading can arise, for instance, if the towfish does not have a heading compass, if the compass malfunctions, or if an improper magnetic declination is used. Additionally, an analyst unaware of this possible discrepancy may inadvertently use the ship's course when geocoding. Finally, a systematic up or down pitch of the towfish also gives rise to position errors if this is not taken into account.

9.4 Bathymetric Correlation

One method that is used to empirically calculate the relative position of the towfish with respect to the ship is to perform a spatial correlation between bathymetry data from a hull-mounted multibeam system and bathymetry data from a bathymetric sidescan system (Fig. 42). Past work using only SeaBeam multibeam bathymetry track crossings indicate that this correlation can resolve the relative positions on the order of 30 m under ideal conditions. These conditions include the presence of sufficient 2-D bathymetric features with adequate relief in the survey area. For bathymetric sidescan data, the combination of overall poorer precision and accuracy of the depth measurements with the need to use empirical lookup angle tables limits the spatial correlation to at best a 30 m error.

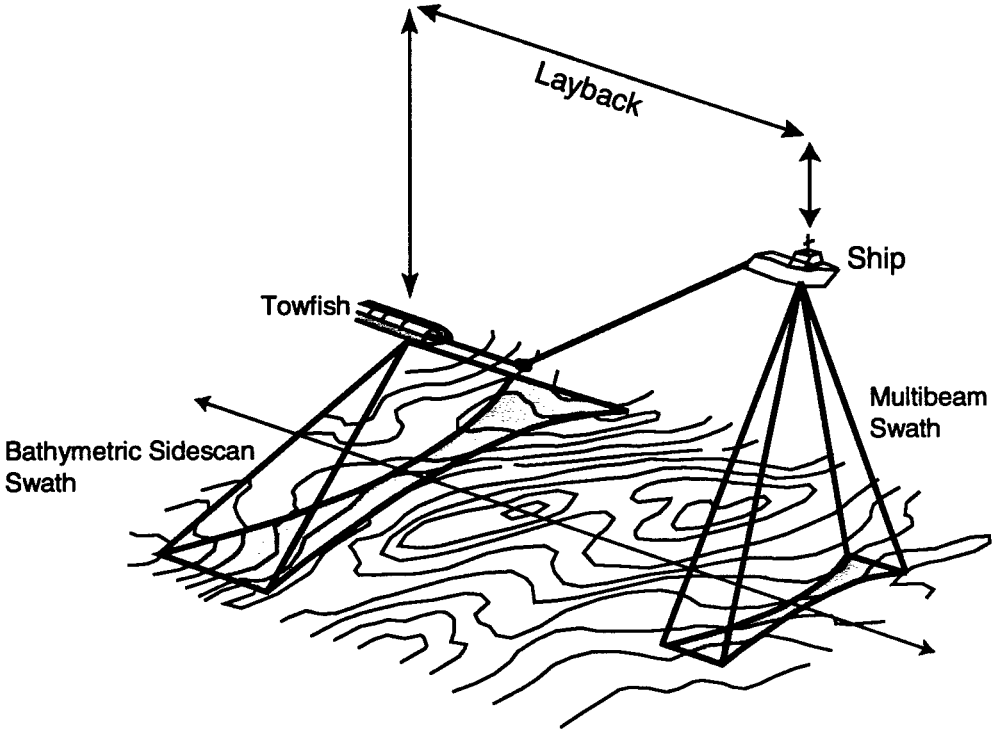

Fig. 42 — Using bathymetric correlation to compute the towfish relative position with respect to the ship. If the ship maintains a constant heading, then the bathymetric sidescan eventually maps out a similar area that was previously mapped by the multibeam system.

The methodology for computing the towfish's relative position with respect to the ship is similar to computing track crossing errors. First, the bathymetry collected by the ship's multibeam system needs to be either gridded or contoured to produce data vectors. Given an estimate of the layback of the towfish and knowledge of the towing speed, a time-lag factor is then computed. The bathymetric data collected by the sidescan system at this later time are then gridded. A spatial correlation between the two bathymetric grids is performed and the best shift computed.

Assuming a relatively constant towing speed and a constant layback factor, the results from the spatial correlation give the error associated with the assumed layback. If a constant length of tow cable is deployed, it is anticipated that the layback correction factor will vary according to changes in towing speed. Additionally, the towing direction and speed with respect to the prevailing current's direction and speed also affects the layback correction. As the standard surveying mode is to run parallel tracks, two sets of layback corrections are sometimes required for the tracks running in the opposite directions.

Another means of obtaining an estimate of the layback position of the towfish is to match features on adjacent overlapping tracks (Fig. 43). This is similar to the bathymetric matching except it uses only the imagery data. If the proper layback value is used, the geocoded position of a target is the same for both tracks. One should keep in mind that there is stretching of the feature due to the finite horizontal beamwidth and that the flat-bottom assumption potentially introduces errors in the position of the target.

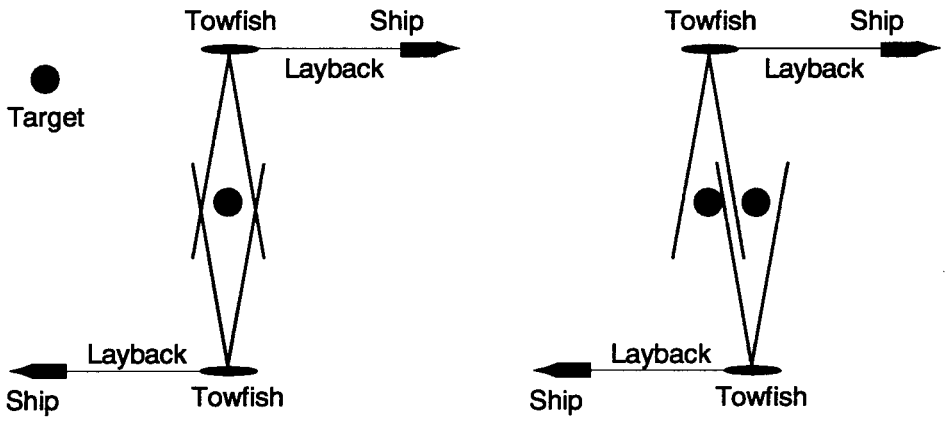

Fig. 43 — Computing layback by matching features on adjacent tracks. The left figure shows an identical positioning of a target when the correct layback correction is used. The right figure shows a mismatch caused by using an incorrect layback value.

9.5 Short-Baseline Systems

The position of a towed system can be ascertained by using a short- or ultra-short baseline system. These positioning systems require an acoustic source (pinger) mounted on the towfish and a receiving array mounted on the towing platform. The proper use of this type of system greatly improves the estimation of the relative position of towfish and, hence, negates one of the sources of position errors.

A short baseline system uses the measured travel-time of a pulse transmitted by the pinger on the towfish to the receiving hydrophones. Using this range information and the geometry of the receivers, triangulation is then performed to obtain an estimate of the towfish's relative position. This calculation is improved by also incorporating the towfish's depth, which is measured using pressure sensors. Additional azimuthal information is obtained if the phase difference of the signal received by the different hydrophones is measured. A conversion from the electrical phase angle to the geometric angle is subsequently computed in the same manner as a bathymetric sidescan system.

9.6 Hull-Mounted System Platform Stability

From an operational perspective, imagery data from hull-mounted multibeam systems should be more accurately positioned than that of towed sidescan systems. However, a more accurate statement would be that the transmit and receive positions of the hull-mounted instrument are more accurately known. Other contributing factors such as refraction effects, platform instability, and beam steering can be major contributors to position inaccuracies if they are not properly considered.

Hull-mounted multibeam systems transmit and receive acoustic information that has propagated through the surface thermocline, which is characterized by significant changes in the sound speed. This results in the refraction of the outgoing and incoming acoustic signal, and contributes to the mislocation of the data in the across-track direction. Note that the majority of ocean surveys are carried out during periods when weather conditions are favorable. Invariably, this time period is the summer months when the thermocline is the most pronounced (i.e., it produces greater refractive effects).

Another contributing source of position errors in multibeam derived data is beam steering used to compensate for pitch and yaw motions [106]. In this technique, which is incorporated in the vast majority of multibeam systems, onboard sensors monitor the pitch and yaw motion of the ship. Using specialized hardware and software control, the transmit beam is electronically steered such that the main lobe is focused in the vertical direction under the ship. Unfortunately, this does not mean that the entire horizontal beam pattern is aligned perpendicularly to ship. Instead, the outer edges of the transmit beam are skewed in the fore-aft direction. Position shifts on the order of hundreds of meters are possible for the data at the outer edges of a 120° swath.

9.7 Across-Track Error: Flat-Bottom Assumption

Time-dependent raw acoustic time-series data need to be converted to across-track pixel values. The methodology used for this conversion, which differs between multibeam and sidescan systems, can introduce errors in the across-track positioning that depends on the accuracy of the transformation parameters. For the case of sidescan systems, these parameters are the depth of the seafloor and the sound speed.

A common method used to compute the across-track pixel values is the flat-bottom assumption (Fig. 21). In this algorithm, it is assumed that the across-track seafloor depths are a constant value. Furthermore, these constant across-track depths are assumed to be the same as the depth directly underneath the towfish. The across-track position x is simply

$$x = \sqrt{r^2 - z^2}\ , \tag{49}$$

where z is the depth as computed from first bottom detect and r is the slant range. If the seafloor is not flat or if the computed bottom-detect depth is incorrect, the across-track position is in error. If one selects a constant sound speed, the previous equation can be rewritten in terms of the slant range travel times t and the bottom-detect time t_o,

$$x = c\sqrt{t^2 - t_o^2} \ . \tag{50}$$

9.7.1 Across-Track Depth Variation / Bottom-Detect Error

It is necessary to know the depth of the seafloor to convert acoustic intensity as a function of time to intensity as a function of across-track distance. For many sidescan systems, the basis for this conversion is the altitude of the towfish over the seafloor, which is computed using detected time of first arrival from the nadir reflection signal. This parameter is usually computed using the time of the first acoustic signal that exceeds some user-defined amplitude threshold.

Two principal problems arise with bottom detect. If the surface of the seafloor is acoustically transparent, the returned signal from reflections off the seafloor may be below the user-defined threshold. Equivalently, this threshold may have been set too high, which results in a late bottom detect. The second problem arises when seafloor beneath the towfish is characterized by a large bathymetric gradient. In this case, the bottom detect signal may not necessarily be from directly beneath the towfish, but may be from an upslope area (Fig. 44).

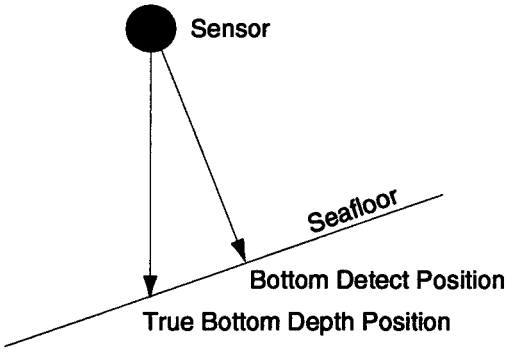

Fig. 44 — How a sloping bottom under the towfish can influence the first reflection return

Across-track range errors caused by inaccuracies in the bottom-detect t_o, and across-track depth variations are similar. They are computed by first taking the derivative of Eqs. (49) and (50);

$$\frac{\partial x}{\partial t_o} = \frac{c t_o}{\sqrt{t^2 - t_o^2}}$$

$$\frac{\partial x}{\partial z} = \frac{z}{\sqrt{r^2 - z^2}} = \tan^{-1}(\theta) \ . \tag{51}$$

The across-track range errors Δx are then given by

$$\Delta x = \frac{\partial x}{\partial t_o}\Delta t_o = \frac{c t_o \Delta t_o}{\sqrt{t^2 - t_o^2}} = \frac{z_o \Delta z_o}{x}$$

$$\Delta x = \frac{\partial x}{\partial z}\Delta z = \frac{z \Delta z}{\sqrt{r^2 - z^2}} = \frac{z \Delta z}{x} . \qquad (52)$$

It is readily apparent from these simple relationships that errors in the across-track range Δx are inversely proportional to the across-track range. This means that the magnitude of these errors is greater for positions at the inner edges of the track (Fig. 45). Conversely, the across-tracks errors are linearly related to the water depth.

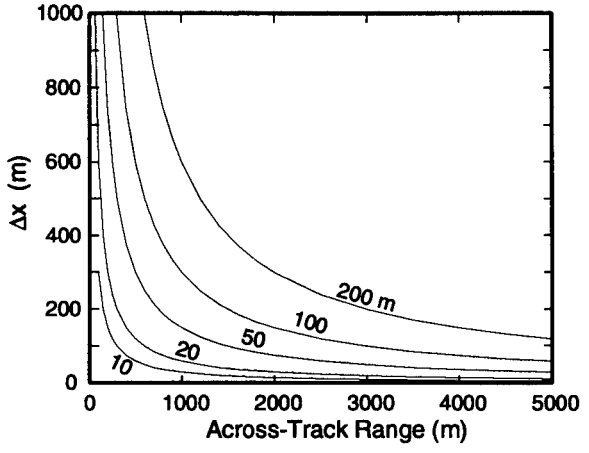

Fig. 45 — Across-track errors as a function of across-track range. This plot is for variations in the depth of seafloor that differ from that of the assumed depth of 3000 m. Errors in range are greatest close to the nadir and diminish towards the outer edge of the track.

9.7.2 Errors Due To Sound Speed

The conversion of time to distance requires knowledge of the sound speed of the propagation medium. For the case of the flat-bottom assumption, errors in the assumed sound speed relate to errors in the across-track position as

$$\frac{\partial x}{\partial c} = \sqrt{t^2 - t_o^2}$$

$$\Delta x = \frac{\partial x}{\partial c}\Delta c = \Delta c\sqrt{t^2 - t_o^2} = x\frac{\Delta c}{c} . \qquad (53)$$

The errors in the across-track position are linearly proportional to the across-track range and errors in the sound speed (Fig. 46). This means that the effect of inaccuracies in the assumed sound

speed is greater at the outer edges of coverage. One point to remember, however, is that the speed of sound in the oceans is fairly well known, and that it does not vary considerably (<10%). Hence, it is relatively simple to select an appropriate value for the sound speed that minimizes the magnitude of this source of position error.

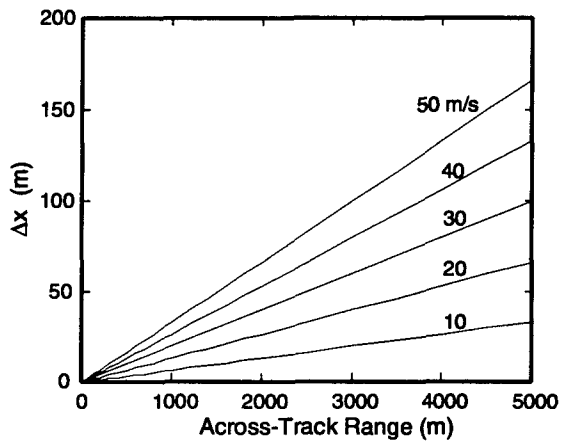

Fig. 46 — Across-track errors as a function of across-track range. This plot shows the range errors caused by errors in the assumed sound speed. Errors increase linearly as a function of across-track range. Water depth for this example is 3000 m with an assumed sound speed of 1500 m/s. Note that the vertical scale of this plot is different than that of Fig. 45.

9.8 Refraction

The speed of sound in the oceans varies as a function of depth, and therefore, the propagation path of the ensonifying and return acoustic energy is not a straight line. This refractive effect is usually not factored into the initial computation for the across-track pixel location, and therefore, errors in position can be introduced by deficiencies in using the straight line assumption. As demonstrated here, refractive effects contribute to the mislocation of the across-track position of imagery data differently for sidescan and multibeam systems.

To illustrate refraction effects, the straight line and refracted propagation paths are shown in Fig. 47 for a summer sound speed profile for a location near Iceland. The source is placed at 90 m, which is typical of a deployed low-frequency sidescan system. As can be seen, the two sets of ray paths diverge for shallower take-off angles. At first glance, it would appear the positioning of the sidescan imagery in the across-track direction would be correspondingly mislocated. However, what is not displayed in these types of ray trace diagrams are the travel-times for the paths. For sidescan systems, this travel time (slant range) is more important than the actual path, as time is the value used to compute x.

This point is more clearly demonstrated by computing the difference between the travel-time for the straight line and refracted paths for a given across-track range. It is important to remember that this across-track position is intercepted by ray paths with two different take-off angles. When the time

difference is computed and converted to across-track range values (Fig. 48), one then observes a relatively small displacement in the across-track range value.

For bathymetric systems, refraction has a direct influence on the across-track range as the position is dependent on the geometry (i.e., take-off angle) of the propagation path (Fig. 47). The depth values are also similarly affected. Another important factor that influences multibeam systems is the presence of the ocean's thermocline where there is a relatively large change in the sound speed due to changes in the vertical temperature structure near the ocean surface. Furthermore, this thermocline is highly seasonal. Sidescan systems are usually deployed at a towing depth at the base of the thermocline and are, therefore, less affected by this change in sound speed.

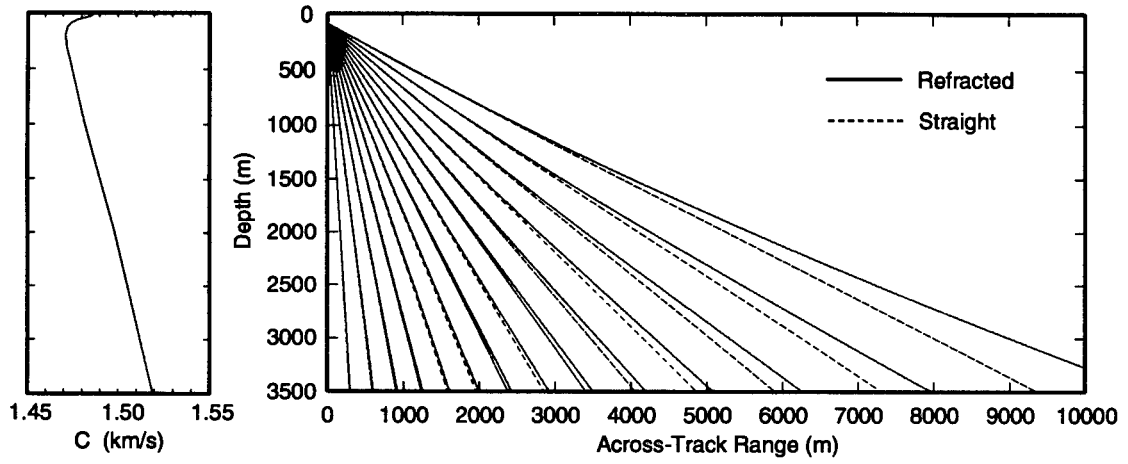

Fig. 47 — Sound speed profile (left) and its associated ray trace diagram. The dashed lines in the right-hand plot represent the straight line path, while the solid lines represent the refracted path. The source depth of 90 m is typical of that for a low-frequency towed sidescan system.

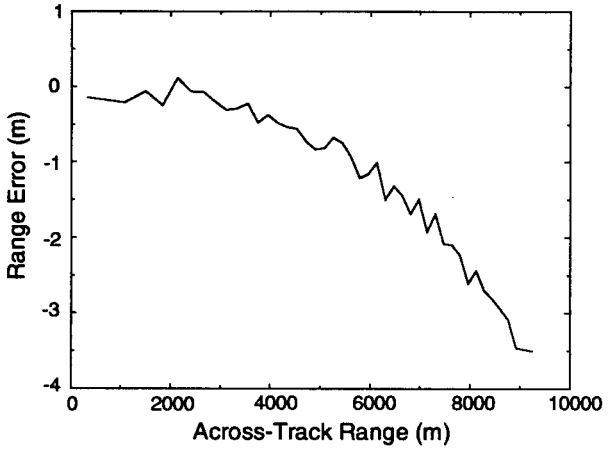

Fig. 48 — Plot of range error vs across track-range. Shown is the difference between the position based on the time of the refracted path minus the position based on the time of the straight line path. The average sound speed is the average for the distribution shown in Fig. 47.

10. ACKNOWLEDGMENTS

This work was funded by the Defense Mapping Agency (now the National Imagery and Mapping Agency). Captain Richard LeRoy and Chris Zavrel are thanked for their support of this project. The Office of Naval Research, of which the Naval Research Laboratory is an activity, provided funding for most of the seafloor imaging surveys in which I have been a scientific participant.

The information contained in this report is a product of countless discussions with many colleagues who willingly passed on to me their ideas and comments on the subject of acoustic backscatter. Much thanks goes to Peter Vogt, Michael Czarnecki, Joan Gardner, Henry Fleming, Dan Chayes, Chris Jones, Christian deMoustier, Steve Lingsch, Alexander (Sandy) Shor, Margo Edwards, John Sender, Karen Sender, Mark Rognstad, Stan Zisk, Gail Yamada, Chris Fox, Haru Matsumoto, Joe Gettrust, Ken Stewart, and Pierre Cervenka.

REFERENCES

1. M.L. Somers and A.R. Stubbs, "Sidescan Sonar," *IEE Proc.* **131**, Part F, 243–256 (1984).
2. E.E. Davis, R.G. Curie, B.S. Sawyer, and J.G. Kosalos, "The Use of Swath Bathymetric and Acoustic Image Mapping Tools in Marine Geoscience," *Mar. Technol. Soc. J.* **20**, 17–27 (1986).
3. M.C. Kleinrock, "Capabilities of Some Systems Used to Survey the Deep-Sea Floor," in *CRC Handbook of Geophysical Exploration at Sea, Hard Minerals,* 2nd ed., R.A. Geyer, ed. (CRC Press, Boca Raton, 1992) pp. 35–56.
4. R.C. Tyce, "Deep Seafloor Mapping Systems – A Review," *Mar. Technol. Soc. J.* **20**, 4–16 (1986).
5. P.R. Vogt and B.E. Tucholke, "Imaging the Ocean Floor: History and State of the Art," in *The Geology of North America, Vol. M: The Western North Atlantic Region*, P.R. Vogt and B.E. Tucholke, eds. (Geological Society of America: Boulder, CO, 1986) pp. 19–44.
6. O. Leenhardt, "Side Scanning Sonar – A Theoretical Study," *Inter. Hydro. Rev.* **51**, 61–80 (1974).
7. B.W. Flemming, "Side-Scan Sonar: a Practical Guide," *Inter. Hydro. Rev.* **53**, 65–92 (1976).
8. H.P. Johnson and M. Helferty, "The Geological Interpretation of Sidescan Sonar," *Rev. Geophys.* **28**, 357–380 (1990).
9. W. Kunze, "General Aspects of Application of Horizontal Echo Sounding Method to Shipping," *Inter. Hydro. Rev.* **34**, 63–72 (1957).
10. E. Aherns, "Use of Horizontal Sounding for Wreck Detection," *Inter. Hydro. Rev.* **34**, 73–81 (1957).
11. W.D. Chesterman, P.R. Clynick, and A.H. Stride, "An Acoustic Aid to Sea Bed Survey," *Acustica* **8**, 285–290 (1958).
12. A.H. Stride, "A Linear Pattern on the Sea Floor and its Interpretation," *J. Mar. Biol. Assoc. UK* **38**, 313–318 (1959).
13. A.R. Stubbs, "Identification of Patterns on Asdic Record," *Inter. Hydro. Rev.* **40**, 53–68 (1963).
14. D.T. Donovan, and A.H. Stride, "An Acoustic Survey of the Sea Floor South of Dorsett and its Geological Interpretation," *Phil. Trans. R. Soc.* **B244**, 299–330 (1961).
15. M.J. Tucker, and A.R. Stubbs, "A Narrow-Beam Echo-Ranger for Fishery and Geological Investigations," *Brit. J. Appl., Phys.* **12**, 103–110 (1961).
16. R.G. Haines, "Developments in Ultrasonic Instruments," *Inter. Hydro. Rev.* **40**, 49–57 (1963).
17. C.S. Clay, J. Ess, and I. Weisman, "Lateral Echo Sounding of the Ocean Bottom on the Continental Rise," *J. Geophys. Res.* **69**, 3823–3835 (1964).
18. J.S.M. Rusby, R. Dobson, R.H. Edge, F.E. Pierce, and M.L. Somers, "Records Obtained from the Trials of a Long-Range Side-Scan Sonar (G.L.O.R.I.A. Project)," *Nature* **223**, 1255 (1969).

19. S. Rusby, "A Long Range Side-Scan Sonar for Use in the Deep Sea (GLORIA Project)," *Inter. Hydro. Rev.* **47**, 25–39 (1970).

20. M.L. Somers, "Signal Processing in Project GLORIA: A Long Range Sidescan Sonar," *Proc. IERE Conf. Electron. Eng. Ocean Tech.*, 109–120 (1970).

21. A.S. Laughton, "The First Decade of GLORIA," *J. Geophys. Res.* **86**, 11511–11534 (1981).

22. EEZ-SCAN 84 Scientific Staff, "Atlas of the Exclusive Economic Zone, Western Conterminous United States," *U.S. Geol. Surv. Misc. Invest. Ser.*, I–1792, 1986.

23. EEZ-SCAN 86 Scientific Staff, "Atlas of the Exclusive Economic Zone, Gulf of Mexico, and Eastern Caribbean Areas," *U.S. Geol. Surv. Misc. Invest. Ser.*, I–1864, 1988.

24. W.D. Chesterman, J.M.P. St Quinton, Y. Chan, and H.R. Matthews, "Acoustic Surveys of the Sea Floor Near Hong Kong," *Inter. Hydro. Rev.* **44**, 35–54 (1967).

25. M.J.P. Heaton and W.G. Haslett, "Interpretation of Lloyd Mirror in Sidescan Sonar," *Proc. Soc Underwater Tech.* **1**, 24–38 (1971).

26. A.R. Stubbs, B.S. McCartney, and J.G. Legg, "Telesounding, A Method of Wide Swathe Depth Measurement," *Inter. Hydro. Rev.* **51**, 23–59 (1974).

27. P.N. Denbigh, "Phase Only Side-Scan Sonar for Underwater Mapping," *Acoust. Lett.* **1**, 84–87 (1977).

28. P.N. Denbigh, "Stereoscopic Visulization and Contour Mapping of the Sea Bed Using a Bathymetric Sidescan Sonar (BASS)," *Radio Elect. Eng.* **53**, 301–307 (1983).

29. D.M. Hussong and P. Fryer, "Back-Arc Seamounts and the Seamarc II Seafloor Mapping System," *EOS Trans. AGU* **64**, 627–632 (1983).

30. J.G. Blackinton, D.M. Hussong, and J. Kosalos, "First Results from a Combination of Side-Scan Sonar and Seafloor Mapping System (SeaMARC II)," *Proc. Offshore Technology Conference*, OTC 4478 **1**, 307–311 (1983).

31. J.G. Blackinton, *Bathymetric Mapping with Seamarc II: An Elevation-Angle Measuring Side-Scan Sonar System*, Ph.D. Thesis (University of Hawaii, Honolulu, 1986) 145 pp.

32. R.J. Babb, "Feasibility of Interferometric Swath Bathymetry Using GLORIA, a Long-Range Sidescan," *IEEE J. Oceanic Eng.* **14**, 299–305 (1989).

33. R. Beale and M. Somers, "Deep Ocean Bathymetric Imaging with GLORI-B," *Proc. ICIP–94* **1**, 886–880 (1994).

34. M.F. Glenn, "Introducing an Operational Multi-Beam Array Sonar," *Inter. Hydro. Rev.* **47**, 35–39 (1970).

35. C. de Moustier, "Inference of Manganese Nodule Coverage from Sea Beam Acoustic Backscattering Data," *Geophysics* **50**, 989–1001 (1985).

36. C. de Moustier, "Beyond Bathymetry: Mapping Acoustic Backscattering from the Deep Seafloor with Sea Beam," *J. Acoust. Soc. Am.* **79**, 316–331 (1986).

37. C. de Moustier, "Approaches to Acoustic Backscattering Measurements from the Deep Seafloor," *J. Energy Resources Tech.* **110**, 77–84 (1988).

38. C. de Moustier, "State of the Art in Swath Bathymetry Survey Systems," *Inter. Hydro. Rev.* **65**, 25–54 (1988).

39. K.K. Talukdar, W. Capell, and C. Zabounidis, "Sidescan Survey Results from a Multibeam Sonar System – Sea Beam 2000," *Mar. Geod.* **15**, 63–79 (1992).

40. E. Hammerstad, F. Pohner, F. Parthiot, and J. Bennett, "Field Testing of a New Deep Water Multibeam Echo Sounder," *Proc. IEEE Oceans'91*, 743–749 (1991).

41. E. Hammerstad, S. Asheim,K. Nilsen, and H. Bodholt, "Advances in Multibeam Echo Sounder Technology," *Proc. IEEE Oceans'93* **1**, 482–487 (1993).

42. J.H. Satriano, L.C. Smith, and J.T. Ambrose, "Signal Processing for Wide Swath Bathymetric Sonars," *Proc. IEEE Oceans'91*, 558–561 (1991).

43. S.C. Lingsch and C.S. Robinson, "Acoustic Imagery Using a Multibeam Bathymetric System," *Mar. Geod.* **15**, 81–95 (1992).

44. R.J. Urick, *Principles of Underwater Sound,* 3rd ed., (McGraw-Hill, New York, 1983).

45. I. Tolstoy and C.S. Clay, *Ocean Acoustics: Theory and Experiments in Underwater Sound*, (McGraw-Hill, New York, 1966).

46. C.S. Clay and H. Medwin, *Acoustical Oceanography: Principles and Applications*, (John Wiley & Sons, New York, 1977).

47. W.M. Carey, "Standard Definitions for Sound Levels in the Oceans," *IEEE J. Oceanic Eng.* **20**, 109–113 (1995).

48. Lord Rayleigh, *Theory of Sound,* 2nd ed. (Dover, New York, 1945).

49. R.W. Leonard, P.C. Combs, and L.R. Skidmore, "Attenuation of Sound in Synthetic Sea Water," *J. Acoust. Soc. Am.* **21**, 63 (1949).

50. W.M. Ewing, W.S. Jardetzky, and F. Press, *Elastic Waves in Layered Media*, (McGraw-Hill, New York, 1957).

51. L. Brekhovskikh and Yu. Lysanov, *Fundamentals of Ocean Acoustics*, (Springer-Verlag, Berlin, 1982).

52. J.A. Ogilvy, "Wave Scattering from Rough Surfaces," *Rep. Prog. Phys.* **50**, 1553–1608 (1987).

53. D.R. Jackson, D.P. Winebrenner, and A. Ishimaru, "Application of the Composite Roughness Model to High-Frequency Bottom Scattering," *J. Acoust. Soc. Am.* **79**, 1410–1422 (1986).

54. C.J. Oliver, "Information from SAR Images," *J. Phys. D, Appl. Phys.* **24**, 1493–1514 (1991).

55. J.V. Gardner, M.E. Field, H. Lee, B.E. Edwards, D.G. Mason, N. Kenyon, and R.B. Kidd, "Ground-Truthing 6.5 Khz Side Scan Sonographs: What Are We Really Imaging?," *J. Geophys. Res.* **96**, 5955–5974 (1991).

56. A.P. Lyons, *Modeling Acoustic Backscatter from the Seafloor by Long-Range Side-Scan Sonar*, M.S. Thesis (Texas A&M University, 1991) 77 pp.

57. A.N. Shor, "Seamarc II Seafloor Mapping System: Seven Years of Pacific Research," *Proc. Pacific Rim 90 Congress* (1990).

58. J.G. Blackinton, D.M. Hussong, and J. Steenstrup, "Seafloor Cable Surveys: Swath Bathymetry from a 'Fish'," *Sea Technology*, 33–39 (1991).

59. D.M. Graham, "Seven-Vessel Fleet Marks Russian CGGE," *Sea Technology* **35**, 67–69 (1994).

60. T.W.C. Hilde, R.L. Carlson, P. Devall, J. Moore, P. Alleman, C.J. Sonnier, M.C. Lee, C.N. Herrick, F. Dwan, and C.W. Kue, "TAMU^2– Texas A&M University Topography and Acoustic Mapping Undersea System," *Proc. IEEE Oceans'91*, 750–755 (1991).

61. R.M. Hubbard, "On the Towfish Motion Characteristics of Single-Body vs. Two-Body Sidescan Systems," *Proc. IEEE Oceans'93* **1**, 365–370 (1993).

62. M. Gutberlet and H. Werner Schenke, "HYDROSWEEP: New Era in High Precision Bathymetric Surveying in Deep and Shallow Water," *Mar. Geod.* **13**, 1–23 (1989).

63. J.A. Grant and R. Schreiber, "Modern Swathe Sounding and Sub-Bottom Profiling Technology for Research Applications: The Atlas Hydrosweep and Parasound Systems," *Mar. Geophys. Res.* **12**, 9–19 (1990).

64. W. Capell and K. Kiesel, "An Extended Capability Multibeam Bathymetric Mapping System," *Proc. IEEE Oceans'89*, 1124–1136 (1989).

65. R.E. Williams, "Creating an Acoustic Synthetic Aperture in the Ocean," *J. Acoust. Soc. Am.* **60**, 60–73 (1976).

66. V.S. Riyait, M.A. Lawlor, A.E. Adams, O. Hinton, and B. Sharif, "Real-Time Synthetic Aperture Sonar Imaging Using a Parallel Architecture," *IEEE Trans. Image Proc.* **4**, 1010–1019 (1995).

67. E.J. Sullivan, W.M. Carey, and S. Sterigiopoulos, "Guest Editorial for: Special Issue on Acoustic Synthetic Aperture Processing," *IEEE J. Oceanic Eng.* **17**, 1–7 (1992).

68. J. Andrews and P. Humphrey, "Swathmap – Long Range Sidescan Sonar Mapping of the Deep Seafloor", *Mar. Geod.* **4**, 141 (1980).

69. P. Alais, F. Ollivier, P. Cervenka, N. Cesbron, and P. Challande, "A High Resolution Sidescan Sonar," *Proc. IEEE Oceans'94* **1**, 340–343 (1994).

70. C.G. Fox, F.J. Jones, and T.-K. Lau, "Constrained Iterative Deconvolution Applied to Seamarc I Sidescan Sonar Imagery," *IEEE J. Oceanic Eng.* **15**, 24–31 (1990).

71. W.S. Burdic, *Underwater Acoustic System Analysis*, 2nd ed. (Prentice Hall, Englewood Cliffs, 1991).

72. J.-M. Augustin, "Side Scan Acoustic Images Processing Software," *Proc. IEEE Oceans'86*, 221–228 (1986).

73. D.D. Bergersen, "A Synopsis of Seamarc II Side-Scan Processing Techniques," *Proc. IEEE Oceans'91*, 921–926 (1991).

74. P. Cervenka and C. de Moustier, "Sidescan Sonar Image Processing Techniques," *IEEE J. Oceanic Eng.* **18**, 108–122 (1993).

75. P.S. Chavez, "Processing Techniques for Digital Sonar Images from GLORIA," *Photogrammetry Eng.* **52**, 1133–1145 (1986).

76. D.A. Chayes, C.E. Nishimura, M.F. Czarnecki, and D. Pitcher, "A Paradigm for Processing Sidescan and Bathymetry Data: The Next Generation," *Proc. MTS'91* **1**, 388-391 (1991).

77. R. Davis, S. Zisk, M. Simpson, M. Edwards, A. Shor, and E. Halter, "Hawaii Mapping Research Group Bathymetric and Sidescan Data Processing," *Proc. IEEE Oceans'93* **2**, 449–453 (1993).

78. D. Johnson, "Side Scan Sonar Imagery Analysis Techniques," *Proc. IEEE Oceans'91*, 935–941 (1991).

79. M.C. Kleinrock, "Overview of Sidescan Sonar Systems and Processing," *Proc. IEEE Oceans'91*, 77–83 (1991).

80. T.P. Le Bas, D.C. Mason, and N.C. Millard, "TOBI Image Processing – The State of the Art," *IEEE J. Oceanic Eng.* **20**, 85–93 (1995).

81. B.P. Luyendyk, E.J. Hajic, and D.S. Simonett, "Side-Scan Sonar Mapping and Computer-Aided Interpretation in the Santa Barbara Channel, California," *Mar. Geophys. Res.* **5**, 365–388 (1983).

82. A. Malinverno, M.H. Edwards, and W.B.F. Ryan, "Processing of Seamarc Swath Sonar Data," *IEEE J. Oceanic Eng.* **15**, 14–23 (1990).

83. R.L. Miller, F.S. Dwan, and C.-F. Cheng, "Digital Preprocessing Techniques for GLORIA II Sonar Images," *Geo-Mar. Lett.* **11**, 23–31 (1991).

84. T.B. Reed IV and D.M. Hussong, "Digital Image Processing for Enhancement and Classification of Seamarc II Side-Scan Sonar Imagery," *J. Geophys. Res.* **94**, 7469–7490 (1989).

85. T.B. Reed IV and B.E. Tucholke, "Geologic Visualization of the Kane Fracture Zone: Interactive Processing of Sidescan and Bathymetric Data," *Proc. IEEE Oceans'93*, 1152–1158 (1993).

86. R.C. Searle, T.P. Le Bas, N.C. Mitchell, M.L. Somers, L.M. Parson, and P. Patriat, "GLORIA Image Processing: The State of the Art," *Mar. Geophys. Res.* **12**, 21–39 (1990).

87. K.K. Talukdar and R.C. Tyce, "Digital Processing of Sidescan Images from Bottom Backscatter Data Collected by Sea Beam," *Mar. Geod.* **14**, 81–100 (1990).

88. Thoros, E.I., "The Validity of the Kirchhoff Approximation for Rough Surface Scattering Using a Gaussian Roughness Spectrum," *J. Acoust. Soc. Am.* **83**, 78–92, 1988.

89. T.-K. Lau, and C.G. Fox, "A Technique for Combining Seamarc I Sidescan Sonar and Gridded Bathymetric Data to Display Undistorted Seafloor Images," *Proc. IEEE Oceans'91*, 1140–1145 (1991).

90. R. Li, "Correction of Pixel Locations of Sidescan Sonar Images Using Bathymetric Data Acquired Separately," *Mar. Geod.* **15**, 211–213 (1992).

91. P.C. Cervenka, C. de Moustier, and P.F. Lonsdale, "Geometric Corrections on Sidescan Sonar Images Based on Bathymetry: Applications with Seamarc II and Sea Beam Data," *Mar. Geophys. Res.* **16**, 365–383 (1994).

92. C. de Moustier and M.C. Kleinrock, "Bathymetric Artifacts in Sea Beam Data: How to Recognize Them and What Causes Them," *J. Geophys. Res.* **91**, 3407–3424 (1986).

93. H. Matsumoto, "Characteristics of Seamarc II Phase Data," *IEEE J. Oceanic Eng.* **15**, 350–360 (1990).

94. P.N. Denbigh, "Swath Bathymetry: Principles of Operation and an Analysis of Errors," *IEEE J. Oceanic Eng.* **14**, 289–298 (1989).

95. P.N. Denbigh, "Signal Processing Strategies for a Bathymetric Sidescan Sonar," *IEEE J. Oceanic Eng.* **19**, 382–390 (1994).

96. C. de Moustier, "Signal Processing for Swath Bathymetry and Concurrent Seafloor Acoustic Imaging," in *Acoustic Signal Processing for Ocean Exploration*, J.M.F. Moura and I.M.G. Lourtie, eds. (Kluwer Academic Publishers, 1993), pp. 329–354.

97. M.A. Masnadi-Shiraz, C. de Moustier, P. Cervenka, and S.H. Zisk, "Differential Phase Estimation with the Seamarc II Bathymetric Sidescan Sonar System," *IEEE J. Oceanic Eng.* **17**, 239–251 (1992).

98. P. Cervenka and C. de Moustier, "Postprocessing and Corrections of Bathymetry Derived from Sidescan Sonar Systems: Application with Seamarc II," *IEEE J. Oceanic Eng.* **19**, 619–629 (1994).

99. D.C. Mason, T.P. Le Bas, I. Sewell, and C. Angelikaki, "Deblurring of GLORIA Side-Scan Sonar Images," *Mar. Geophys. Res.* **14**, 125–136 (1992).

100. D. Sauter and L. Parson, "Spatial Filtering for Speckle Reduction, Contrast Enhancement, and Texture Analysis of GLORIA Images," *IEEE J. Oceanic Eng.* **19**, 563–576 (1994).

101. C. de Moustier, P.F. Lonsdale, and A.N. Shor, "Simultaneous Operation of the Sea Beam Multibeam Echo-Sounder and the Seamarc II Bathymetric Sidescan Sonar System," *IEEE J. Oceanic Eng.* **15**, 84–94 (1990).

102. T.P. Le Bas and D.C. Mason, "Suppression of Multiple Reflections in GLORIA Sidescan Sonar Imagery," *Geophys. Res. Lett.* **21**, 549–552 (1994).

103. C.E. Nishimura and D.W. Forsyth, "Improvements in Navigation Using Seabeam Crossing Errors," *Mar. Geophys. Res.* **9**, 333–352 (1988).

104. D.T. Cobra, *Estimation and Correction of Geometric Distortions in Side-Scan Sonar Images*, Ph.D. Thesis (Massachusetts Institute of Technology and Woods Hole Oceanographic Institution, 1990).

105. D.T. Cobra, A.V. Oppenheim, and J.S. Jaffe, "Geometric Distortions in Sidescan Images: A Procedure for Their Estimation and Correction," *IEEE J. Oceanic Eng.* **17**, 252–268 (1992).

106. W.J. Capell Sr., C. Zabounidis, and K. Talukdar, "Pitch and Yaw Effects on Very Wide Swath Multibeam Sonars," *Proc. IEEE Oceans'93* **1**, 353–358 (1993).